THE RESPONSE OF STRATOSPHERIC WATER VAPOR TO CLIMATE CHANGE DRIVEN BY DIFFERENT FORCING AGENTS

A Dissertation

by

XUN WANG

Submitted to the Office of Graduate and Professional Studies of
Texas A&M University
in partial fulfillment of the requirements for the degree of

DOCTOR OF PHILOSOPHY

Chair of Committee,	Andrew E. Dessler
Committee Members,	Kenneth Bowman
	John W. Nielsen-Gammon
	Gerald R. North
Head of Department,	Ramalingam Saravanan

December 2020

Major Subject: Atmospheric Sciences

ABSTRACT

We investigate the response of stratospheric water vapor (SWV) to forcing agents with different physical properties within the Precipitation Driver and Response Model Intercomparison Project (PDRMIP) framework. For each model and forcing agent, we break the SWV response into a slow response, which is coupled to surface temperature changes, and a fast response, which is the direct response to external forcing, but without any mediation from the surface temperature. Our results show that, for most climate perturbations, the slow SWV response dominates the long-term change of SWV in both the tropical lower stratosphere (TLS) and the lowermost stratosphere (LMS). The slow SWV component responds to different forcing agents with a similar efficacy. The slow SWV response is largely controlled by the surface temperature, and it exhibits a similar sensitivity across all climate perturbations, which is 0.35 $ppmv\ K^{-1}$ in the TLS, 2.1 $ppmv\ K^{-1}$ in the Northern Hemispheric LMS, and 0.97 $ppmv\ K^{-1}$ in the Southern Hemispheric LMS. Most climate perturbations produce close to zero fast SWV response. The fast SWV response only dominates the slow SWV response when the forcing agent radiatively heats the cold point region – for example, black carbon, which directly heats the atmosphere by absorbing solar radiation. The fast SWV response in the TLS is primarily controlled by the fast adjustment of cold point temperatures across all climate perturbations, with a sensitivity of 0.52 $ppmv$ per degree of cold point warming. This control becomes weaker at higher altitudes and at higher latitudes below 150 hPa.

CONTRIBUTORS AND FUNDING SOURCES

Contributors

This work was supervised by a dissertation committee consisting of Dr. Andrew Dessler, Dr. John Nielsen-Gammon, Dr. Kenneth Bowman, and Dr. Gerald North.

The PDRMIP model data is obtained from the website: https://cicero.oslo.no/en/PDRMIP. We would like to acknowledge the PDRMIP modeling groups for making the data publicly available. We acknowledge helpful discussions with Dr. Andrew Gettelman, Dr. William Randel, Dr. John Nielsen-Gammon, Dr. Kenneth Bowman, and Dr. Gerald North. We acknowledge proofreading by Steven Schroeder.

Dr. Andrew Dessler provided the conceptualization, guidance, and editing of the dissertation. All other work conducted for the dissertation was completed by the student independently.

Funding Sources

This work was supported by NASA grants 80NSSC18K0134 and 80NSSC19K0757. This work was also supported by the National Center for Atmospheric Research, which is a major facility sponsored by the National Science Foundation under Cooperative Agreement No. 1852977. Any opinions, findings and conclusions or recommendations expressed in this material do not necessarily reflect the views of the National Science Foundation.

NOMENCLATURE

ERF	Effective radiative forcing
GHG	Greenhouse gas
LMS	Lowermost stratosphere
NH	Northern hemisphere
SH	Southern hemisphere
SWV	Stratospheric water vapor
TCP	Temperature at the cold point
TLS	Tropical lower stratosphere
TTL	Tropical tropopause layer
TOA	Top of atmosphere

TABLE OF CONTENTS

LIST OF FIGURES

FIGURE Page

LIST OF TABLES

TABLE Page

1. INTRODUCTION AND LITERATURE REVIEW*

Stratospheric water vapor (SWV) plays an important role in global climate change. It is an important greenhouse gas (GHG), which affects the Earth's radiative budget (Forster and Shine, 2002; Solomon et al., 2010), and could exert an important positive feedback to global warming (Forster and Shine, 2002; Dessler et al., 2013; Huang et al., 2016; Banerjee et al., 2019). Changes in stratospheric temperatures resulting from SWV trends may also influence stratospheric circulation (Maycock et al., 2013), and SWV is also important in stratospheric ozone chemistry because it is the major source of hydroxyl (OH) radicals, which play a role in regulation of ozone (e.g. Dvortsov and Solomon, 2001; Solomon et al., 2010).

1.1 Stratospheric water vapor in the overworld and the lowermost stratosphere

The stratosphere can be split into the overworld (above 380-K isentropic surface) (e.g. Hoskins, 1991) and the extratropical lowermost stratosphere (LMS, between the extratropical tropopause and the 380-K isentropic surface) (e.g. Holton et al., 1995; Dessler et al., 1995). Distinct pathways contribute to water vapor in the overworld and the LMS (Fig. 1.1).

Overworld SWV is controlled by two sources: troposphere to stratosphere transport and methane oxidation. Air is transported into the stratosphere through the tropical tropopause layer (TTL) by the wave-driven Brewer-Dobson circulation (BDC) or occasionally by small-scale convective overshooting (Brewer, 1949; Holton et al., 1995; Fueglistaler et al., 2009) (Fig. 1.1a, path A). The TTL is the troposphere to stratosphere transition and

runs from 355 K (150 hPa, 14 km) to 425 K (70 hPa, 18.5 km) potential temperature in the tropics (Sherwood and Dessler, 2000; Fueglistaler et al., 2009) (See shaded region in Fig. 1.1a). The low temperatures of the TTL dehydrates the air that ascents through it, largely determining the amount of water vapor that enters the overworld (Mote et al., 1995, 1996; Fueglistaler et al., 2005; Schoeberl et al., 2008; Fueglistaler et al., 2009). In the upper stratosphere, water vapor is produced in situ from oxidation of methane (e.g. Brasseur and Solomon, 2005).

The LMS SWV is contributed by three major sources. The first is the overworld air transported poleward and downward into the LMS by the BDC (Dessler et al., 1995; Holton et al., 1995; Plumb, 2002; Gettelman et al., 2011) (Path A in Fig. 1.1b). The second is the adiabatic isentropic transport from the upper troposphere to the LMS (Path B in Fig. 1.1b). The subtropical jet forms a transport barrier between the upper troposphere and the LMS due to the strong gradient in potential vorticity (Chen, 1995; Haynes and Shuckburgh, 2000), producing a correspondent gradient in trace gases (Pan et al., 1997; Richard, 2003; Ray, 2004). Thus isentropic mixing between the troposphere and the LMS occurs at regions around the jet when baroclinic instability and wave breaking occurs (e.g. Plumb, 2002; Gettelman et al., 2011). The third is the cross-tropopause diabatic transport by deep convection (Path C in Fig. 1.1b). Both observations and models show evidence of convective injection of water vapor into the LMS (Wang, 2003; Dessler and Sherwood, 2004; Ray, 2004; Lane and Sharman, 2006; Hanisco et al., 2007; Mullendore et al., 2009; Hassim and Lane, 2010).

1.2 Climate change concepts

The Earth and its atmosphere absorb shortwave radiation from the sun and emit longwave radiation to space. When the planet is at its radiative equilibrium, the net incoming solar radiation equals outgoing longwave radiation. Climate perturbations occur when a

difference between the net incoming solar radiation and the outgoing longwave radiation is imposed - this is known as a radiative forcing. The factors that drive the radiative forcing are called forcing agents and these can be natural or anthropogenic perturbations in a radiatively active constituent of the atmosphere, in the planet's albedo, or in the amount of insolation.

How one defines radiative forcing is important when different forcing agents with different physical properties are investigated. Traditionally, studies calculate the instantaneous radiative forcing, which is the instantaneous change in the net radiation flux at the tropopause or the top of atmosphere (TOA) resulting from a forcing agent. However, forcing agents can influence the atmosphere before the surface temperature changes. This occurs on a time scale of weeks to months and is often referred to as an "adjustment" to the forcing (e.g. Sherwood et al., 2015). Previous studies refer to the change in the Earth?s net radiative flux before the surface temperature changes but after the atmosphere adjusts to the external forcing as the effective radiative forcing (ERF). It accounts for the direct forcing from the perturbation as well as the contribution by the atmospheric adjustment. Recent studies show that ERF provides a more comprehensive understanding of the Earth?s energy budget when investigating different climate perturbations (e.g. Sherwood et al., 2015; Richardson et al., 2019).

Different forcing agents result in different atmospheric adjustments. For example, increased GHGs cools the stratosphere, requiring the surface and troposphere to warm more to balance the instantaneous radiative forcing (Hansen et al., 1997). This results in a positive contribution to the radiative forcing. It is shown that tropospheric temperature, stratospheric temperature, cloud, and etc. all adjust distinctly to different forcing agents and contribute differently to the radiative forcing (Smith et al., 2018).

Different climate forcing agents affect the climate differently. For example, an increase in GHGs results in increased absorption of longwave radiation emitted from the surface

and troposphere. This reduces the outgoing longwave to space and warms the surface (Jain et al., 2000). Sulfate aerosols, on the other hand, cool the surface by scattering solar radiation directly or indirectly through cloud nucleation and formation (Ramanathan, 2001). Nevertheless, Richardson et al. (2019) show that the global surface temperature response per unit of ERF is basically the same for different forcing agents.

1.3 The response of stratospheric water vapor to climate change

Given the importance of stratospheric water vapor to our climate system, it is of great interest for the climate community to understand potential stratospheric water vapor responses in a changing climate. Like radiative forcing, the response of SWV to climate change can be partitioned into two components: the fast response and slow response. The fast response is akin to the adjustments to the forcing, as discussed in Section 1.2, which is the response to the perturbation before the surface temperature changes (e.g. Sherwood et al., 2015). The slow response is the component in the SWV change that is coupled with the surface temperature change, which occurs on longer time scales. This slow response means that SWV could be an important positive feedback to global warming (Forster and Shine, 2002; Dessler et al., 2013; Huang et al., 2016; Banerjee et al., 2019). Banerjee et al. (2019) have shown that, when CO_2 is abruptly quadrupled, the change in SWV mainly consists of the slow response and the fast response is less important.

Previous studies have shown that climate models, which are able to accurately reproduce the observed interannual variations in SWV (Dessler et al., 2013; Smalley et al., 2017), robustly project a positive long-term trend in overworld SWV in the tropical lower stratosphere under a scenario with increasing GHGs (Gettelman et al., 2010; Dessler et al., 2013; Smalley et al., 2017). This is mainly due to a warmer tropopause (Thuburn and Craig, 2002; Gettelman et al., 2010; Lin et al., 2017; Smalley et al., 2017; Xia et al., 2019), which is controlled, to some extent at least, by the radiative effect of a warming

surface (Gettelman et al., 2010; Shu et al., 2011; Dessler et al., 2013; Huang et al., 2016; Revell et al., 2016; Lin et al., 2017; Smalley et al., 2017; Banerjee et al., 2019).

Dessler et al. (2016) suggest that increases in convective injection into the stratosphere may also be contributing to the trend in water vapor entering the tropical lower stratosphere. Methane oxidation contributes to the trend in the SWV at higher altitudes, but has little impact on the trend in SWV at the entry levels (Hegglin et al., 2014; Revell et al., 2016). In the LMS, the climate models show that, when CO_2 increases, the SWV has a larger positive trend and it is at least partly contributed by the warming troposphere (Dessler et al., 2013; Huang et al., 2016; Banerjee et al., 2019).

These previous studies are based on a climate change pattern mainly or entirely forced by increasing CO_2. However, different climate forcing agents result in different patterns of climate change depending on their physical properties. It is not clear, if perturbed separately, whether they all affect SWV similarly. The goal of this study is to investigate the response of both overworld and LMS SWV to forcing agents with different physical properties.

1.4 Motivation and dissertation outline

SWV plays an important role in climate change, thus its potential future trend is of great interest to the climate community.

In this dissertation, we investigate SWV response in a multi-model and multiple forcing agent framework. We aim to answer these questions:

1) What are the magnitudes of fast and slow responses in SWV when forced by different forcing agents?

2) Which is more important, the fast or slow SWV response when forced by different forcing agents?

3) Is the relationship between the SWV response and surface temperature change ro-

bust across different forcing agents and models?

4) What drives the fast response?

5) Is the fast response robust across different forcing agents and models?

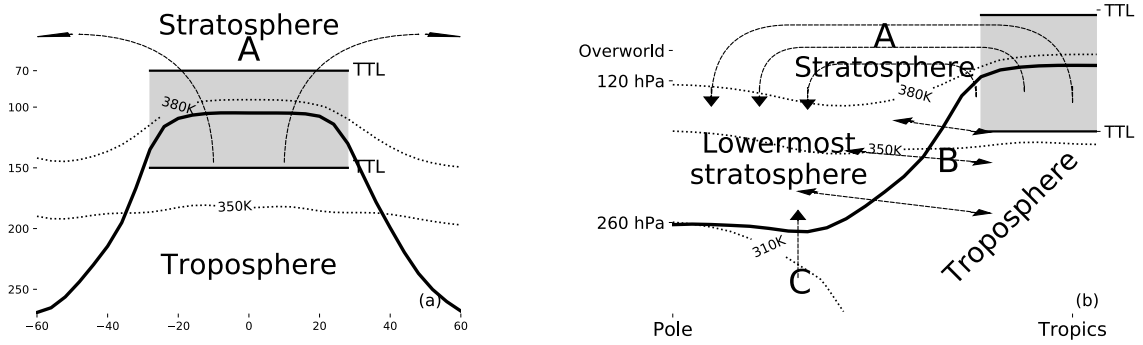

Figure 1.1: (a) Schematic of the tropical tropopause layer and transport between troposphere and stratosphere. (b) Schematic of the stratospheric overworld and lowermost stratosphere. We produced a schematic using European Centre for Medium-Range Weather Forecasts (ECMWF) ERA-Interim potential temperature, tropopause, and pressure climatology data. The heavy line is the tropopause. This is similar to Figure 1 of Dessler et al. (1995). Dotted lines are isentropic surfaces. The arrows are schematics to show the transport pathways. See text for description of paths A, B, and C.

2. METHOD*

2.1 The PDRMIP set-up

In this dissertation, we analyze output produced by nine models from the Precipitation Driver and Response Model Intercomparison Project (PDRMIP) (Samset et al., 2016; Myhre et al., 2017; Tang et al., 2018, 2019). These are Climate Model Inter-comparison Project phase 5 (CMIP5) era models (Table 2.1) and each performed a baseline and multiple climate perturbation experiments (Table 2.1). The PDRMIP data can be downloaded from this website: https://cicero.oslo.no/en/PDRMIP.

In the perturbation experiments, perturbations on a global scale are applied abruptly at the beginning of the model simulation. The five core experiments include a doubling of CO_2 concentration ($2\times CO_2$), a tripling of CH_4 concentration ($3\times CH_4$), a 2% increase in solar irradiance (2%Solar), an increase of present-day black carbon concentration or emission by factor of 10 (10×BC), and an increase of present-day SO_4 concentration or emission by factor of 5 ($5\times SO_4$). Apart from the five core experiments, some of the climate models also performed additional perturbation experiments. These include an increase in CFC-11 concentration from 535 ppt to 5 ppb (hereafter, 10×CFC-11), an increase in CFC-12 concentration from 653.45 ppt to 5 ppb (hereafter, 10×CFC-12), an increase in N_2O concentration from 316 ppb to 1 ppm (hereafter, $3\times N_2O$), an increase in year 2000 tropospheric O_3 concentration used in MacIntosh et al. (2016) by factor of 5 ($5\times O_3$), and an increase of present-day black carbon with shorter lifetime by factor of 10 (10×BCSLT). Table 2.1 provides details about the models and the perturbations each one simulated.

*This dissertation is adapted with permission under the Creative Commons Attribution 4.0 License (https://creativecommons.org/licenses/by/4.0/) from "The response of stratospheric water vapor to climate change driven by different forcing agents" by Xun Wang and Andrew Dessler, 2020, preprinted in *Atmospheric Chemistry and Physics Discussion*, 2020, 1-22, Copyright [2020] by Copernicus Publications and the authors of the manuscript and its final journal article.

The perturbations in GHGs and solar irradiance are relative to the models' baseline simulations. In the baseline simulations, the concentration of the GHGs and solar irradiance are at present-day levels, except for HadGEM2, which is at pre-industrial level. The perturbations in the aerosols depend on whether it is possible to prescribe aerosol concentrations in the models. For models that are able to prescribe aerosol concentrations, the aerosol perturbations are based on a multi-model mean baseline aerosol concentration in 2000 obtained from the AeroCom Phase II initiative (Myhre et al., 2013). For those that are only able to produce aerosols through emissions, the perturbation is applied by increasing the emissions by the factors listed above. The 10×BCSLT experiment is performed only by models that are able to prescribe aerosol concentrations.

Each perturbation experiment and each baseline simulation are performed in two configurations: A simulation with fixed sea surface temperatures and sea-ice ("fixed SST") and a simulation that is fully coupled (slab ocean for CAM4 only). The fixed SST simulations use the SST and sea-ice climatology at either present-day level or pre-industrial level (HadGEM2). The fixed SST simulations are at least 15 years and the coupled simulations are at least 100 years.

2.2 Fast response and slow response

When available, SWV mixing ratio is obtained directly from the specific humidity output by each model simulation. For the models that do not output specific humidity (CAM5, GISS-E2-R, and MIROC-SPRINTARS), we calculate specific humidity by multiplying the models' relative humidity with respect to ice by the saturation mixing ratio with respect to ice calculated using model temperature and pressure.

We define ΔSWV, the change in SWV mixing ratio in response to a particular perturbation, to be the difference between SWV in the perturbed coupled run and that in the baseline coupled run. As discussed above, the ΔSWV can then be broken down into

the two components: the fast response (ΔSWV_{fast}) and slow response (ΔSWV_{slow}). We compute results at each zonal mean latitude and pressure level and results averaged in the tropical lower stratosphere (70 hPa, 30°N-30°S, hereafter, TLS), in the northern hemispheric (NH) lowermost stratosphere (50°N-90°N at 200 hPa, hereafter, NH LMS), and in the southern hemispheric (SH) lowermost stratosphere (50°S-90°S at 200 hPa, hereafter, SH LMS). Most previous studies have focused on response of water vapor in the TLS (e.g., Gettelman et al., 2010; Shu et al., 2011; Smalley et al., 2017). But recent studies report that the climate is most sensitive to changes in water vapor in the LMS (Solomon et al., 2010; Dessler et al., 2013; Banerjee et al., 2019), so we also investigate that region.

We use the fixed SST simulations to compute ΔSWV_{fast}, the change in SWV before the surface temperature changes. ΔSWV_{fast} is the difference between the SWV mixing ratio in the fixed SST run with the forcing perturbation and that in the fixed SST run with the baseline atmosphere, because the SSTs are the same in the two runs, any difference in SWV must be unconnected to surface temperature changes. Most models reach equilibrium after 5 years, so we use the ΔSWV_{fast} averaged during the last 10 years of the model run in this dissertation.

We calculate ΔSWV_{slow} as ΔSWV minus ΔSWV_{fast}. To estimate the time series of ΔSWV_{slow}, we use annual mean ΔSWV over the entire coupled run period (at least 100 years) minus the ten-year average ΔSWV_{fast}. Figure 2.1 shows the annual mean ΔSWV_{slow} at 70 hPa averaged over 30°N-30°S for all perturbed simulations and models. It takes models millennia to reach equilibrium, so we expect it to take this long for ΔSWV_{slow} to reach equilibrium.

Because of this, we estimate equilibrium ΔSWV_{slow} using a regression method similar to the methodology introduced by Gregory et al. (2004). The basic concept is that we regress the annual mean global average net downward radiative flux (R) at the top of atmosphere (TOA) against the annual mean ΔSWV at each zonal mean latitude and pressure

level and annual mean ΔSWV averaged at TLS, NH LMS, or SH LMS. The equilibrium ΔSWV is where the linear fit intercepts at R=0. Then we simply subtract ΔSWV_{fast} from the equilibrium ΔSWV to estimate equilibrium ΔSWV_{slow}.

These regressions can be very noisy and yield highly uncertain parameters, particularly for perturbations with relatively small amounts of radiative forcing and warming. To account for this, we first fit the R and ΔSWV time series using an exponential function ($y(t) = b + a1 \cdot e^{-t/\tau 1} + a2 \cdot e^{-t/\tau 2}$), and then do the regression using the fitted time series. For fully coupled models, we constrain $\tau 1$ to be within the range of 4$\pm$2 years and $\tau 2$ to be within the range of 250$\pm$70 years; for CAM4, in which the atmosphere is coupled to a slab ocean, we constrain $\tau 1$ to be within the range of 4$\pm$2 years. We use HadGEM3 2xCO_2 R and ΔSWV time series as examples to show this calculation (Fig. 2.2). We then compute the best fit of all parameters. The ranges for the time constants are based on previous estimations of climate system time scales (Geoffroy et al., 2013). We estimate the ΔSWV-intercept at R=0 by regressing the fitted R and ΔSWV data over the last 30 years, since the relation between R and ΔSWV is not necessarily linear over the entire 100-year period. The difference between the equilibrium ΔSWV_{slow} obtained using this method and the ΔSWV_{slow} averaged over the last 30 years is mostly on the order of 0.01-1 ppmv, except for a few outliers (Fig. 2.3). The slow and fast responses of other variables, such as surface temperatures and cold point temperatures are computed using the same method.

We tested this method in a climate model that nearly reaches the equilibrium climate state. We analysed runs of the fully coupled Max Planck Institute Earth System Model version 1.1 (MPI-ESM1.1) (Maher et al., 2019), which has a transient climate response and an effective climate sensitivity near the middle of the CMIP5 ensemble range (Adams and Dessler, 2019; Dessler, 2020). It includes a 2000-year preindustrial control run and a 2614-year abruptly quadrupled CO_2 run. The values of ΔSWV averaged over the last 30

years of the $4 \times CO_2$ run relative to the control run are 4.60 ppmv in the TLS, 22.40 ppmv in the NH LMS, and 9.69 ppmv in the SH LMS. We expect this to be close to equilibrium ΔSWV because the trend in global average surface temperature over the last 500 years of the $4 \times CO_2$ run is 0.02 K per century. We use the regression method to estimate the equilibrium ΔSWV using MPI-ESM1.1 water vapor mixing ratio time series over the first 100 years and obtain estimates of 4.38 ppmv in the TLS, 20.01 ppmv in the NH LMS, and 9.07 ppmv in the SH LMS; these yield differences of 0.22 ppmv in the TLS, 2.39 ppmv in the NH LMS, and 0.62 ppmv in the SH LMS. Thus, our method underestimates the true equilibrium value by 5% in the TLS, 11% in the NH LMS, and 6% in the SH LMS.

2.3 Ensemble average and Uncertainty

When we discuss the ensemble average and uncertainty of a response, e.g. ΔSWV, for a perturbation experiment in this dissertation, the uncertainty is obtained from Monte Carlo calculations as follows: We sample results from each model that performed that perturbation with replacement 100,000 times; from these samples, we compute the 2.5%-97.5% percentiles of the ensemble mean.

We also discuss the ensemble average and uncertainty of a regression slope for a perturbation experiment. The uncertainty of the ensemble average slope produced by a perturbation is also obtained from Monte Carlo calculations: For each model and perturbation, we first randomly sample the slope 100,000 times, assuming a Gaussian distribution set by the standard deviation estimated from a t-test. Then, for each perturbation, we sample from the slope distributions with replacement 100,000 times for each model that performed that perturbation and from these samples compute the 2.5%-97.5% percentiles of the ensemble mean.

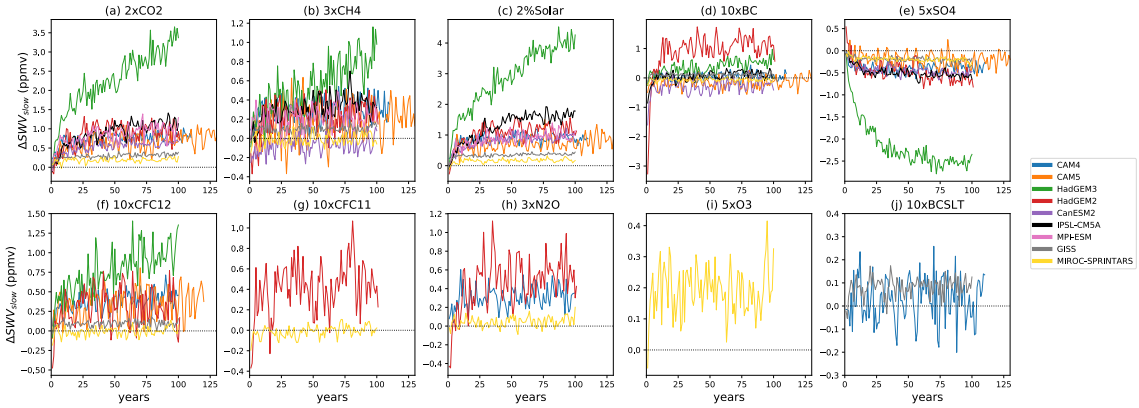

Figure 2.1: Annual mean ΔSWV_{slow} (ppmv) at 70 hPa averaged between 30ºN and 30ºS, starting from the 1st year to the end of each model run. The model runs are at least 100 years. The color coding indicates results from different models.

Table 2.1: Description of PDRMIP models (Table 3 from Myhre, G., and Coauthors, (2017). PDRMIP: A Precipitation Driver and Response Model Intercomparison Project - Protocol and Preliminary Results. *Bulletin of the American Meteorological Society*, 98(6):1185 - 1198. https://doi.org/10.1175/BAMS-D-16-0019.1. © American Meteorological Society. Used with permission.) and list of perturbation experiments used in this study (last column).

Model	Version	Resolution	Ocean setup	Aerosol setup	Key references	Perturbation experiments
Second Generation Canadian Earth System Model (CanESM2)	2010	2.8°×2.8°, 35 levels	Coupled ocean	Emissions	(Arora et al., 2011)	2xCO_2, 3xCH_4, 2%Solar, 10xBC, 5xSO_4

Table 2.1 continued

Model	Version	Resolution	Ocean setup	Aerosol setup	Key references	Perturbation experiments
Community Earth System Model, version 1 (Community Atmosphere Model, version 4) [CESM1(CAM4)]	1.0.3	2.5°×1.9°, 26 levels	Slab ocean	Fixed concentrations	(Neale et al., 2010; Gent et al., 2011)	2xCO_2, 3xCH_4, 2%Solar, 10xBC, 5xSO_4, 10xCFC-12, 3xN_2O, 10xBCSLT
CESM1 CAM5	1.1.2	2.5°×1.9°, 30 levels	Coupled ocean	Emissions	(Hurrell et al., 2013; Kay et al., 2015; Otto-Bliesner et al., 2016)	2xCO_2, 3xCH_4, 2%Solar, 10xBC, 5xSO_4, 10xCFC-12
Goddard Institute for Space Studies Model E2, coupled with the Russell ocean model (GISS-E2-R)	E2-R	2°×2.5°, 40 levels	Coupled ocean	Fixed concentrations	(Schmidt et al., 2014)	2xCO_2, 3xCH_4, 2%Solar, 10xBC, 5xSO_4, 10xCFC-12, 10xBCSLT

Table 2.1 continued

Model	Version	Resolution	Ocean setup	Aerosol setup	Key references	Perturbation experiments
Hadley Centre Global Environment Model, version 2—Earth System (includes Carbon Cycle configuration with chemistry) (HadGEM2-ES)	6.6.3	1.875°×1.25°, 38 levels	Coupled ocean	Emissions	(Bellouin et al., 2011; Collins et al., 2011)	2xCO_2, 3xCH_4, 2%Solar, 10xBC, 5xSO_4, 10xCFC-12, 10xCFC-11, 3xN_2O
HadGEM3	Global Atmosphere 4.0	1.875°×1.25°, 85 levels	Coupled ocean	Fixed concentrations	(Bellouin et al., 2011; Walters et al., 2014)	2xCO_2, 3xCH_4, 2%Solar, 10xBC, 5xSO_4, 10xCFC-12
L'Institut Pierre-Simon Laplace Coupled Model, version 5A (IPSL-CM5A)	CMIP5	3.75° ×1.875°, 39 levels	Coupled ocean	Fixed concentrations	(Dufresne et al., 2013)	2xCO_2, 3xCH_4, 2%Solar, 10xBC, 5xSO_4

Table 2.1 continued

Model	Version	Resolution	Ocean setup	Aerosol setup	Key references	Perturbation experiments
Max Planck Institute Earth System Model (MPI-ESM)	1.1.00p2	T63, 47 levels	Coupled ocean	Climatology, year 2000	(Giorgetta et al., 2013)	2xCO_2, 3xCH_4, 2%Solar
Model for Interdisciplinary Research on Climate-Spectral Radiation-Transport Model for Aerosol Species (MIROC-SPRINTARS)	5.9.0	T85 (approx. 1.4°×1.4°), 40 levels	Coupled ocean	Hemispheric Transport Air Pollution, phase 2 Emissions	(Takemura, 2005; Takemura et al., 2009; Watanabe et al., 2010)	2xCO_2, 3xCH_4, 2%Solar, 10xBC, 5xSO_4, 10xCFC-12, 10xCFC-11, 3xN_2O, 5xO_3

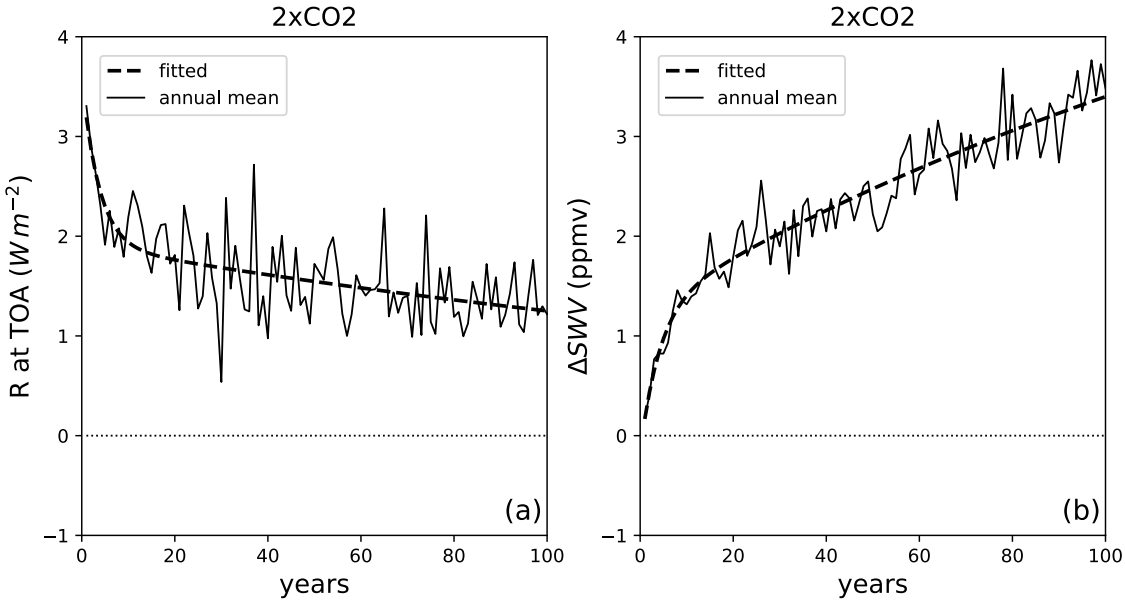

Figure 2.2: Panel (a): Annual mean global average R at TOA (Wm^{-2}), starting from the 1st year to the end of each model run, shown as the solid line. Panel (b): Annual mean total ΔSWV (ppmv) at 70 hPa averaged between 30°N and 30°S, starting from the 1st year to the end of each model run, shown as the solid line. The dashed lines are the fitted curve obtained using the method discussed in Section 2.2.

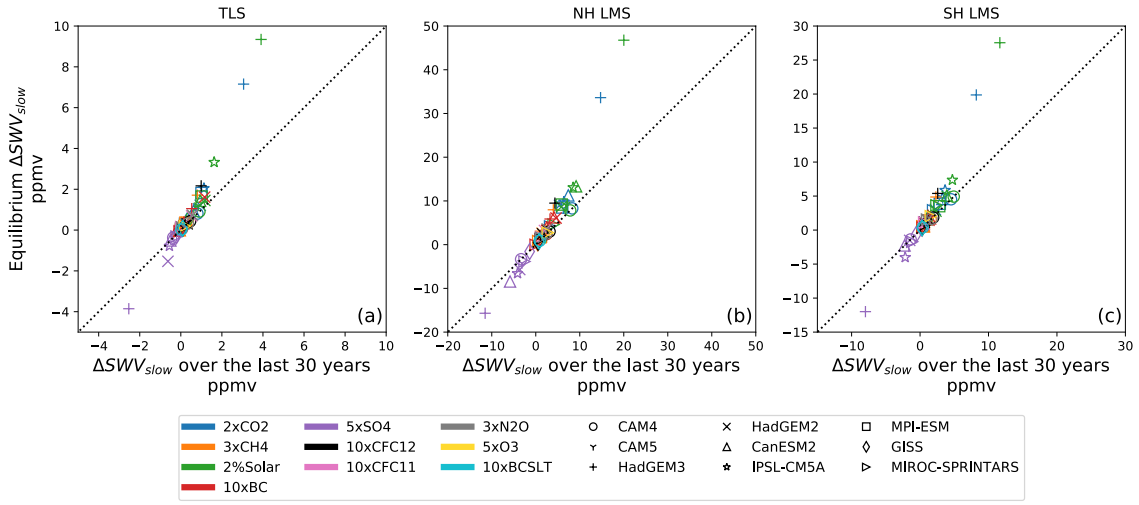

Figure 2.3: Scatter plot of equilibrium ΔSWV_{slow} (ppmv) obtained using the method described in Section 2.2 vs. the ΔSWV_{slow} (ppmv) averaged over the last 30 years of the model run. The color coding indicates results from different perturbations. Marker shapes indicate results from different models.

3. RESULTS*

3.1 Climate change patterns forced by the 10 forcing agents

To give some context to the various climate perturbations, we first show the effective radiative forcing (ERF) and surface temperature change from each climate perturbation, which are important quantities to evaluate climate change. Figure 3.1 shows the zonal mean ERF from all models and perturbations. ERF is the difference in net radiation at the top of atmosphere (TOA) after the atmospheric perturbation (e.g., the addition of CO_2), but before the surface has changed. In all cases, we calculate this by differencing the average of the last 10 years of the fixed SST run with the perturbed atmosphere from the same quantity in the fixed SST run with the baseline atmosphere. In addition, we also show the zonal mean equilibrium surface temperature changes in Fig. 3.2, calculated using the method described in Section 2.2.

Different perturbations show distinct characteristics. Most forcing agents that affect longwave radiation, including $2\times CO_2$, $3\times CH_4$, 10×CFC-11, 10×CFC-12, and $3\times N_2O$ show stronger ERF in the tropics compared to higher latitudes (Figs. 3.1a, b, f, g, and h). This is due to the surface temperature latitudinal gradient. The higher surface temperature in the tropics results in larger longwave absorption in the atmosphere.

Note that $5\times O_3$ does not show the same latitudinal gradient as other longwave forcing agents (Fig. 3.1i). This is because the tropospheric O_3 is transported into the extratropical LMS. O_3 in the LMS absorbs shortwave radiation, so an increase in O3 increases absorption of solar radiation at higher latitudes. Therefore, for $5\times O_3$, there is an increase in

*This dissertation is adapted with permission under the Creative Commons Attribution 4.0 License (https://creativecommons.org/licenses/by/4.0/) from "The response of stratospheric water vapor to climate change driven by different forcing agents" by Xun Wang and Andrew Dessler, 2020, preprinted in *Atmospheric Chemistry and Physics Discussion*, 2020, 1-22, Copyright [2020] by Copernicus Publications and the authors of the manuscript and its final journal article.

energy into the system in the tropics through longwave absorption and at higher latitudes through shortwave absorption.

The forcing agents that affect shortwave radiation, including 10×BC, 5×SO_4, and 10×BCSLT show larger magnitudes of ERF in the Northern Hemisphere than in the tropics and Southern Hemisphere (Figs. 3.1d, e, j, and k). This occurs because most emissions occur in the Northern Hemispheric continents (Myhre et al., 2017). Sulfate aerosols cool the surface by scattering solar radiation (Figs. 3.2e and k) (Ramanathan, 2001), while black carbon reduces the planet's albedo and warms the planet by absorbing solar radiation in the atmosphere and over snow and sea ice surfaces (Figs. 3.1d and j) (Ramanathan, 2001; Ramanathan and Carmichael, 2008).

2%Solar affects shortwave radiation by increasing the solar radiation. It does not change the concentration of any radiative active constituents. The latitude distribution of the increase in solar radiation follows the cosine of latitude (Fig. 3.1c), as expected. More solar radiation is received by the planet around the equator, which results in maximum ERF in the tropics and weaker ERF at higher latitudes. Although the ERF from 2%Solar shows a similar latitudinal pattern compared to 2×CO_2 (Fig. 3.1a and c), previous studies show that changing insolation drives different circulation responses compared to increasing CO_2 (Guo et al., 2018).

The equilibrium surface temperature change (Fig. 3.2) from all climate perturbations and models show stronger response at higher latitudes, especially in the Northern Hemisphere. The larger response at higher latitudes, known more generally as polar amplification, is due to the snow and ice feedback there (e.g. Rind, 2008). The larger response in the Northern Hemisphere compared to the Southern Hemisphere corresponds to more land than ocean (Friedman et al., 2013). In addition, the ocean meridional overturning circulation also transports heat to the Northern Hemisphere from Southern Hemisphere, contributing to the asymmetry in the temperature response (Friedman et al., 2013).

Figure 3.3a shows the global average ERF (values for each model and perturbation are listed in Table A-1). Overall, there is good agreement between different models for each perturbation. We also compare global average warming per unit forcing in Fig. 3.3b (also see Table A1). $\Delta Ts/ERF$ is the inverse of the feedback parameter λ (e.g. Dessler and Zelinka, 2015), so Fig. 3.3b implies that the climate sensitivity to these different perturbations is similar. Our result is consistent with (Richardson et al., 2019).

5×O_3 and 10×BCSLT produce smaller $\Delta Ts/ERF$ values. This may be due to a lower efficacy for these perturbations. However, MIROC-SPRINTARS is the only model in this study that performed 5×O_3, and it also produces low efficacy for all other climate perturbations. Only two models performed 10×BCSLT, so it is also uncertain whether the efficacy forced by 10×BCSLT is robustly smaller than other climate perturbations.

3.2 The slow stratospheric water vapor response

Figure 3.4 shows the ensemble average zonal mean equilibrium ΔSWV_{slow} for each perturbation. Since the vertical gradient of water vapor is large, we show the percentage change (%) of mixing ratio relative to the baseline. In order to compare the magnitudes of responses across different perturbations, we also normalize the equilibrium ΔSWV_{slow} using ERF, so differences in the magnitude of the forcing do not confound our results. Note that this flips the sign of the response to 5×SO_4. It shows that there is an overall moistening in the stratosphere, with strongest response close to the tropopause. The maximum moistening is in the tropical upper troposphere, which is the main part of the tropospheric water vapor feedback. On average, the stratosphere between tropopause and 10-hPa level at all latitudes on average moistens by 0.33±0.09 $ppmv/(Wm^{-2})$ and 7.80±2.00 %/(Wm^{-2}) for all the perturbations. The zonal mean equilibrium $\Delta SWV_{slow}/ERF$ also show general agreement in the patterns across different climate perturbations.

Figure 3.5 shows the ensemble average zonal mean equilibrium temperature slow re-

sponse in the atmosphere (ΔT_{slow}) normalized by ERF from all perturbations. We use lapse rate tropopause, the lowest level where the lapse rate decreases to 2 $K\,km^{-1}$, to show the distinction between troposphere and stratosphere. The lapse rate tropopause is obtained using the atmospheric temperatures from the baseline coupled run and ensemble averaged. These plots show maximum warming in the tropical upper troposphere, extending into the TTL. The warming in the TTL is what causes the positive ΔSWV_{slow} in the overworld.

Previous studies show that the warming TTL is radiatively heated by the warming surface and local radiatively active constituents when GHGs increases (Gettelman et al., 2010; Shu et al., 2011; Dessler et al., 2013; Huang et al., 2016; Revell et al., 2016; Lin et al., 2017; Smalley et al., 2017; Banerjee et al., 2019). All perturbations show the "bull horn" pattern of warming extending upward and poleward from the subtropical tropopause. This pattern is also shown in climate models under a 4xCO4 climate forcing reported by Huang et al. (2016), who pointed out that it is dynamically driven by the strengthened BDC. The general agreement in the magnitude and pattern of $\Delta SWV_{slow}/ERF$ and $\Delta T_{slow}/ERF$ across different climate perturbations indicates that the ΔSWV_{slow} is driven by similar mechanisms despite being forced by different forcing agents.

The magnitudes of the $\Delta SWV_{slow}/ERF$ in the LMS close to the tropopause from most simulations are generally larger than those in the tropical lower stratosphere (Fig. 3.4). This is consistent with previous studies, which showed that the long-term trend in SWV over the 21st century in climate models is largest in the LMS (Dessler et al., 2013; Huang et al., 2016; Banerjee et al., 2019). This also reflects different transport pathways into the LMS compared to the TLS, which is controlled by multiple factors, including the downward transport by the Brewer-Dobson circulation, quasi-horizontal isentropic mixing from the tropical troposphere, and convective influence (Dessler et al., 1995; Holton et al., 1995; Plumb, 2002; Gettelman et al., 2011).

It is also noteworthy that the zonal mean equilibrium $\Delta SWV_{slow}/ERF$ shows a hemispheric asymmetry for all perturbations. In the LMS, the $\Delta SWV_{slow}/ERF$ is larger in the Northern Hemisphere than the Southern Hemisphere. This is consistent with previous studies (Dessler et al., 2013; Banerjee et al., 2019) and is likely due to larger contributions from isentropic transport and convective moistening compared to the Southern Hemisphere (Pan et al., 1997, 2000; Dethof et al., 1999, 2000; Ploeger et al., 2013).

3.3 The slow stratospheric water vapor and ERF

In this section, we use results averaged over selected regions, instead of showing zonal mean results in a latitude-pressure domain. For results in the tropical lower stratosphere (hereafter, TLS), we use ΔSWV_{slow} at 70 hPa, averaged between 30°N and 30°S. As shown in Fig. 3.4, 70 hPa is above the tropical tropopause, so it represents the amount of water vapor entering the tropical overworld. For results in the LMS, we use ΔSWV_{slow} at 200 hPa, averaged between 50°N and 90°N for the Northern Hemisphere (NH), and averaged between 50°S and 90°S for the Southern Hemisphere (SH). We chose this level in the LMS so that it is above the extratropical tropopause and below 100 hPa. However, we note that the water vapor response has a large vertical gradient in the LMS (Fig. 3.4), so our choice of location in the LMS may not be a comprehensive representation of the entire region.

Figure 3.6 shows the equilibrium $\Delta SWV_{slow}/ERF$ in the TLS (Fig. 3.6a), NH LMS (Fig. 3.6b), and SH LMS (Fig. 3.6c) from all models and perturbations (also see Table A-1). Fig. 3.6 is consistent with Fig. 3.4 in that the ensemble average $\Delta SWV_{slow}/ERF$ shows general agreement across different climate perturbations. We also show the percentage contribution of equilibrium ΔSWV_{slow} to the total equilibrium ΔSWV in Figures 3.6d-f. For most perturbations, the equilibrium ΔSWV_{slow} contributes to a major part of the total equilibrium ΔSWV (Figs. 3.6d-f). In the LMS, the ensemble average

$\Delta SWV_{slow}/\Delta SWV$ ratio is close to 100% for many perturbations (Figs. 3.6e-f). In the TLS, the ensemble average $\Delta SWV_{slow}/\Delta SWV$ ratio is generally above 50%, with a few exceptions (10×BC, 10×CFC-11, 10×CFC-12, 5×O_3, and 10×BCSLT). We will discuss these runs in detail in Section 3.5.

Inter-model variability exists in the magnitudes of $\Delta SWV_{slow}/ERF$. The inter-model variability is generally consistent within the ensemble. For example, HadGEM3 generally produces larger responses than the rest of the ensemble, likely connected to larger surface warming per ERF than the rest of the ensemble (Fig. 3.3b). GISS and MIROC-SPRINTARS have $\Delta SWV_{slow}/ERF$ values generally below the rest of the ensemble, likely connected to smaller surface temperature changes per ERF (Fig. 3.3b). We note that MIROC-SPRINTARS has a low top (2.9 hPa), which may affect the stratospheric water vapor response. More work is needed to explain these differences between models, but that is outside of the scope of this study.

Based on the general agreement in the pattern and magnitude of equilibrium ΔSWV_{slow} $/ERF$ across all perturbations (Figs. 3.4-3.6), we regress the ensemble average equilibrium ΔSWV_{slow} of all perturbations against the ensemble average ERF in Figure 3.7. In the TLS (Fig. 3.7a), the water vapor increases 0.35 $ppmv/(Wm^{-2})$, with a 95% confidence interval ranging from 0.17 to 0.53 $ppmv/(Wm^{-2})$. In the LMS (Figs. 3.7b-c), the water vapor increases by 2.15 $ppmv/(Wm^{-2})$ in the NH and increases by 1.18 $ppmv/(Wm^{-2})$ in the SH, with 95% confidence intervals ranging from 1.28 to 3.02 $ppmv/(Wm^{-2})$ in the NH and ranging from 0.76 to 1.61 $ppm/(Wm^{-2})$ in the SH. These regressions indicate that the stratospheric water vapor slow component responds to the different forcing agents with a similar efficacy. Since our Fig. 3.3b shows surface temperature responds to ERF with a similar efficacy for almost all perturbations, this indicates that ΔSWV_{slow} may respond to ΔTs with a similar sensitivity. We will discuss this in detail in the next subsection.

3.4 The slow stratospheric water vapor response and the surface temperature change

Overall, our results show that, in most climate perturbations analyzed in this study, the response of water vapor in both the TLS and the LMS primarily consists of the ΔSWV_{slow}, which is the component mediated by surface temperature change. In addition, Sections 3.1 and 3.3 show that the equilibrium ΔSWV_{slow} and surface temperature respond to the ERF with a similar efficacy across all perturbations analyzed in this study. Previous studies showed that when CO_2 increases, SWV increases due to a warmer tropopause (Thuburn and Craig, 2002; Gettelman et al., 2010; Lin et al., 2017; Smalley et al., 2017; Xia et al., 2019), which is controlled, to some extent at least, by the warming surface (Gettelman et al., 2010; Shu et al., 2011; Dessler et al., 2013; Huang et al., 2016; Revell et al., 2016; Lin et al., 2017; Smalley et al., 2017; Banerjee et al., 2019). To directly quantify how SWV responds to surface temperature across a range of different climate change mechanisms, we linearly regress the annual mean time series of ΔSWV_{slow} against the annual mean time series of global averaged ΔTs over the entire period of the coupled simulation (at least 100 years). This is similar to the analysis of Banerjee et al. (2019), who did this for quadrupled CO_2 perturbation, but we do this for multiple perturbations.

The scatter plot of ΔSWV_{slow} vs. ΔTs for each perturbation and model is shown in Figures 3.8-3.10. In most perturbations and models, the ΔSWV_{slow} time series in both the TLS and the LMS is positively correlated with the ΔTs time series. This supports the hypothesis that the surface temperature change contributes to the long-term trend in SWV for most cases.

Figure 3.11 shows the slopes of the regression between ΔSWV_{slow} and ΔTs annual mean time series for all perturbations and models. We also did the regression using detrended annual ΔSWV_{slow} and annual ΔTs by removing their linear trend, and got similar results (not shown). In all three regions, the slopes from different perturbations show gen-

eral agreement (Fig. 3.11). In the TLS, the ensemble and perturbation average slope is 0.35 $ppmv\,K^{-1}$ with a 95% confidence interval of 0.28-0.44 $ppmv\,K^{-1}$. The LMS ΔSWV_{slow} has stronger correlations with the ΔTs (Fig. 3.11) and produces larger sensitivities. Specifically, the ensemble and perturbation average slope is 2.1 $ppmv\,K^{-1}$ in the NH, and is 0.97 $ppmv\,K^{-1}$ in the SH, with 95% confidence intervals of 1.82-2.39 $ppmv\,K^{-1}$ and 0.79-1.15 $ppmv\,K^{-1}$, respectively. Again the larger LMS SWV sensitivity reflects a different mix of transport pathways into the LMS compared to the TLS (Dessler et al., 1995; Holton et al., 1995; Plumb, 2002; Gettelman et al., 2011).

In order to compare results with previous studies, we also regress the TLS ΔSWV_{slow} annual mean time series against 500-hPa temperature response averaged over 30°N-30°S and regress the LMS ΔSWV_{slow} annual mean time series against the 500-hPa temperature response averaged over 30°N-90°N and 30°S-90°S. These are similar to the regressions done by Dessler et al. (2013) and Smalley et al. (2017) respectively. The ensemble and perturbation average slopes are 0.27$\pm$0.07 $ppmv\,K^{-1}$ in the TLS, 2.0$\pm$0.2 $ppmv\,K^{-1}$ in the NH LMS, and 1.15$\pm$0.13 $ppmv\,K^{-1}$ in the SH LMS. Smalley et al. (2017) gave an ensemble average slope of 0.32$\pm$0.15 $ppmv\,K^{-1}$ for TLS water vapor when the climate is perturbed by projected 21st century forcing. In the regression using observed and reanalysis water vapor data and reanalysis tropospheric temperature, Dessler et al. (2013) reported slope values of 1.1$\pm$0.7 and 0.7$\pm$0.5 $ppmv\,K^{-1}$ in NH and SH, respectively, for the response to interannual variability. In their regression using a chemistry-climate model experiencing the longterm warming under the RCP4.5 scenario, Dessler et al. (2013) reported slope values of 2.9$\pm$0.1 and 1.9$\pm$0.1 $ppmv\,K^{-1}$ in NH and SH, respectively. Our results are in reasonable agreement with Dessler et al. (2013) and Smalley et al. (2017).

The positive correlation and similar SWV sensitivities suggest that not only the surface temperature change contributes to the SWV trend, but SWV also responds to the surface temperature change with a similar sensitivity across a range of different climate change

mechanisms. This also suggests that a positive SWV climate feedback exists not only in a climate change perturbed by increasing CO_2 and GHGs in general (Dessler et al., 2013; Huang et al., 2016; Smalley et al., 2017; Banerjee et al., 2019), but also in a wider range of climate perturbations discussed in this study.

There is clear inter-model variability in the sensitivities. The HadGEM2 10×BC produces a large value of ΔSWV_{slow} sensitivity of 1.78 $ppmv\,K^{-1}$. MIROC-SPRINTARS generally produces extremely small sensitivities in the TLS (Fig. 3.11a, 3.3 and 3.6, Table A-1). The models show better agreement in the TLS but have larger confidence intervals in the LMS. TLS water vapor is mainly controlled by the TTL temperatures, but the LMS water vapor, on the other hand, is controlled by a mix of different factors (Dessler et al., 1995; Holton et al., 1995; Plumb, 2002; Gettelman et al., 2011). The larger inter-model variability in the LMS reflects larger differences in the way models represent these transport pathways.

We also extend the relation between ΔSWV_{slow} and the ΔTs time series to the entire stratosphere in Fig. 3.12. We re-gridded the zonal mean ΔSWV_{slow} annual mean time series from all models and perturbations onto the same pressure-latitude grid (10 hPa above 100 hPa and 50 hPa below 100 hPa, 4 degrees latitude) and regress the ΔSWV_{slow} time series at each grid point against the global average ΔTs time series. The ensemble and perturbation average correlation coefficient and slope of the linear fit at each grid point is shown in Fig. 3.12. Figure 3.13 shows ensemble average slopes for each individual perturbation. Since the vertical gradient of the SWV mixing ratio is large, for Fig. 3.12b and Fig. 3.13, we plot the percentage change of mixing ratio per degree K relative to the baseline.

Our result shows that the ΔSWV_{slow} time series is strongly correlated with the ΔTs time series in both the overworld stratosphere and LMS. Both the correlation coefficient and slope are larger in the LMS than in the tropical overworld. The slope also shows a

hemispheric asymmetry, with larger values in the NH LMS region. This indicates that the NH LMS ΔSWV_{slow} is more sensitive to the surface and tropospheric temperature changes. This is consistent with previous studies, which showed that isentropic transport brings more tropospheric water vapor to the NH than the SH (Pan et al., 1997, 2000; Dethof et al., 1999, 2000; Ploeger et al., 2013). In addition, convective moistening may be more important in the NH due to more land in the NH and, consequently, more convection (Dessler and Sherwood, 2004; Smith et al., 2017; Ueyama et al., 2018; Wang et al., 2019). We note that in Fig. 3.13 the $5\times O_3$ shows weak ΔSWV_{slow} sensitivity to ΔTs in the TLS region. This corresponds to the weak equilibrium TLS ΔSWV_{slow}, which consists a small part in the total equilibrium ΔSWV (less than 30%, Fig. 3.6d).

3.5 The fast stratospheric water vapor response

Figures 3.14-3.16 show the ensemble average zonal mean $\Delta SWV_{fast}/ERF$, ensemble average zonal mean temperature fast response normalized by ERF ($\Delta T_{fast}/ERF$), and $\Delta SWV_{fast}/ERF$ from all models and perturbations averaged in TLS, NH LMS, and SH LMS. ΔSWV_{fast} is the change in SWV due to the atmospheric perturbation, but before the surface temperature has responded. The lapse rate tropopause in Figures 3.14-3.15 is obtained from the baseline fixed SST run averaged during the last 10 years.

Overall, the $\Delta SWV_{fast}/ERF$ is smaller than $\Delta SWV_{slow}/ERF$ for most perturbations in both the TLS and LMS (Figs. 3.16d-f). Given the small values, there is large variability in the magnitudes and contributions of $\Delta SWV_{fast}/ERF$ and ΔSWV_{fast} (Figs. 3.14 and 3.16) across different perturbations, especially in the TLS. This corresponds to the distinct patterns of $\Delta T_{fast}/ERF$ for different perturbations, which shows that the atmosphere responds to the forcing agents differently depending on their radiative properties.

It is generally acknowledged that an increase in CO_2 cools the stratosphere as a rapid

adjustment (Manabe and Wetherald, 1975). This cooling is shown in the $\Delta T_{fast}/ERF$ (Figs. 3.15a and 3.15k). The small magnitude in the ensemble average TLS ΔSWV_{fast} $/ERF$ (Fig. 3.7a) corresponds to close to zero temperature change in the TTL (Figs. 3.15a and 3.15k). This is a result of cancellation between cooling by BDC advection and local radiative heating (Lin et al., 2017). Models including CanESM2, GISS, and MIROC-SPRINTARS even produce cooling and negative $\Delta SWV_{fast}/ERF$ (Fig. 3.16a). In the NH LMS, the $\Delta SWV_{fast}/ERF$ magnitude is also small (Figs. 3.14a and 3.16b-c). This is related to the weak warming in the NH LMS and tropical upper troposphere (Fig. 3.15a).

Compared to $2\times CO_2$, GHG forcing agents including 10xCFC-12 and 10xCFC-11 produce larger magnitudes of $\Delta SWV_{fast}/ERF$ and larger contributions (49% and 55%, respectively) to the total equilibrium ΔSWV in the TLS (Figs. 3.16d). These correspond to the larger heating in the TTL and TLS (Figs. 3.15f, 3.15g and 3.15k). This is because, unlike CO_2, the Halocarbons absorb the upwelling longwave radiation in the atmospheric window range from the troposphere and heat the TTL and TLS (Jain et al., 2000).

$5\times O_3$ is another GHG that shows distinct fast response pattern (Figs. 3.14i and 3.15i). Increases of tropospheric O_3 reduce the radiation absorbed by stratospheric O_3, which cools the stratosphere (Figs. 3.15i and 3.15k). Meanwhile, the O_3 in the upper troposphere absorbs shortwave radiation and heats the TTL (Fig. 3.15i and 3.15k), which results in larger TLS ΔSWV_{fast} magnitude than ΔSWV_{slow} and larger contributions to total equilibrium ΔSWV (77%) (Figs. 3.14i and 3.16a). In the LMS, the tropospheric O_3 is transported there and heats the LMS through short wave radiation absorption (Fig. 3.15i). This also results in larger ΔSWV_{fast} magnitude than ΔSWV_{slow} in both the NH and SH LMS (Fig. 3.16).

The $3\times CH_4$ includes multiple models that produce larger TLS $\Delta SWV_{fast}/ERF$ magnitudes and contributions than $\Delta SWV_{slow}/ERF$ (Figs. 3.14b, 3.16a and 3.16d). This corresponds to larger TTL and TLS heating (Fig. 3.15b and 3.15k). The TTL and

TLS heating could be due to the shortwave radiation absorbed by CH_4, which is explicitly treated in models including CAM5, CanESM2, MPI-ESM, and MIROC-SPRINTARS (Smith et al., 2018). These models are also the ones that produce larger $\Delta SWV_{fast}/ERF$ and larger contributions to the total equilibrium ΔSWV in 3×CH_4 (Figs. 3.16a and 3.16d). There is also less stratospheric cooling compared to 2×CO_2, which could be due to the CH_4 concentration decreasing sharply with altitude in the stratosphere (Hoffmann et al., 2008; Payan et al., 2009; Kellmann et al., 2012).

The ΔSWV_{fast} from 10×BCdominates the total equilibrium ΔSWV in the TLS. The ensemble average ΔSWV_{fast} contributes to 84% of the total equilibrium ΔSWV in the TLS (Fig. 3.16d). The ensemble average $\Delta SWV_{fast}/ERF$ for this perturbation is also larger than any other perturbations in both the tropical overworld and LMS regions (Figs. 3.14d and 3.16). This occurs because the 10×BCstrongly absorbs shortwave radiation, causing large heating of the tropopause region in both the tropics and extra-tropics (Figs. 3.15d and 3.15k). Figure 3.15k shows the fast temperature response of the TTL due to different perturbations and it shows the 10×BCgives by far the most warming per unit ERF. This TTL warming allows more water vapor to enter the TLS and the warming in the LMS also allows more moisture transported from the troposphere (Figs. 3.14d, 3.15d, and 3.16).

The 10×BC$\Delta SWV_{fast}/ERF$ in the NH and SH LMS contributes to about 50% of the total equilibrium ΔSWV, with smaller magnitudes in the SH (Figs. 3.14d and 3.16f). This is because the total amount of prescribed black carbon is smaller in the SH (Myhre et al., 2017), since black carbon is a combustion product and is predominantly emitted over the continents (Ramanathan and Carmichael, 2008). This leads to smaller radiative heating in the SH and correspondingly smaller impact on the fast response there. This also corresponds to the ERF latitudinal pattern (Fig. 3.1d).

The 10×BCSLT is a forcing agent with similar radiative property compared to 10×BC,

which also contributes more than 50% of the total ΔSWV in the TLS and NH LMS. However, the BC in 10×BCSLT is removed by wet deposition, thus has a shorter life time. This results in less heating per unit ERF (Fig. 3.15j) and smaller $\Delta SWV_{fast}/ERF$ compared to 10×BC.

3.6 The fast stratospheric water vapor response and cold point temperature

We show in this section that the ΔSWV_{fast} is closely related to the fast response of atmospheric temperatures (e.g. Mote et al., 1996; Fueglistaler et al., 2009; Lin et al., 2017). We quantify the control of TTL temperature fast adjustments over the TLS ΔSWV_{fast} across a range of different climate change mechanisms by regressing the TLS ΔSWV_{fast} against the fast response of the cold point temperature.

It is well known that the cold point temperature (ΔTCP_{fast}) in the TTL provides one of the fundamental controls on overworld water vapor. To estimate ΔTCP_{fast} in the models, we first find the minimum temperature in the profile at each grid point in the fixed SST runs (no interpolation is done, we simply find the minimum temperature on the output model levels). These minimum temperatures are then averaged between 30°N - 30°S to yield ΔTCP_{fast} in each run. ΔTCP_{fast} is the difference between ΔTCP_{fast} in the perturbed model run minus that in the baseline runs.

We find that TLS ΔSWV_{fast} is strongly correlated with ΔTCP_{fast} across all perturbations and models (Fig. 3.17a), with a slope of 0.52 $ppmv\,K^{-1}$ and a 95% confidence interval of 0.43 to 0.61 $ppmv\,K^{-1}$. Randel and Park (2019) pointed out that the slope from the Clausius-Clapeyron relationship evaluated near the tropical tropopause is about 0.5 $ppmv\,K^{-1}$. The slope from our analysis is consistent with their result.

We also separately do the regression for each individual perturbation and each individual model in the TLS (Fig. 3.17d and 3.17g). For the perturbations that have more than five participating models, including 2×CO_2, 3×CH_4, 2%Solar, 10×BC, 5×SO_4,

and 10×CFC-12, we calculate the linear regression between ΔSWV_{fast} and ΔTCP_{fast} and show the slopes and 95% confidence intervals. For the perturbations that have fewer participating models, including $10 \times 10xCFC11$, 3×N_2O, 5×O_3, and 10×BCSLT, we plot the ratio ΔSWV_{fast}/ΔTCP_{fast} and show only the ensemble averages.

The slopes produced by different perturbations show general agreement (Fig. 3.17d). There is larger uncertainty in the slopes produced by 2%Solar and 10×CFC-12. This is because both the ΔTCP_{fast} and ΔSWV_{fast} in 2%Solar and 10×CFC-12 produced by different models are close and have extremely small standard deviations.

The slopes produced by models generally agree with each other (Fig. 3.17g). The two outliers are HadGEM2 and MPI-ESM. The larger slope produced by HadGEM2 is caused by the large ΔSWV_{fast} from the 10×BCrun. The MPI-ESM performed only three perturbed simulations (2×CO_2, 3×CH_4, and 2%Solar) and their ΔTCP_{fast} and ΔSWV_{fast} values are close to zero, thus resulting in a large ΔSWV_{fast}/ΔTCP_{fast} ratio. To summarize, the fast response of TTL temperature is a good predictor of the tropical LS ΔSWV_{fast} across a range of different climate mechanisms and across multiple models.

In the LMS, ΔSWV_{fast} does not correlate as strong with ΔTCP_{fast} as in the TLS (Figs. 3.17b-c) due to the fact that TTL temperatures are only one factor that influences the LMS. The ΔTCP_{fast} only controls the humidity of overworld air transported poleward and downward by BDC (Dessler et al., 1995; Holton et al., 1995; Plumb, 2002; Gettelman et al., 2011). We leave out the impact of convective transport and isentropic mixing from this linear regression. The direct convective injection of high water vapor does not occur frequently in the observations (Schwartz et al., 2013), and the overall convective contribution to the LMS water vapor is still under debate (e.g., Anderson et al., 2012; Ploeger et al., 2013). The isentropic mixing of tropospheric water vapor into LMS is shown to be important, especially during boreal summer (Dethof et al., 1999; Gettelman et al., 2011; Ploeger et al., 2013), but its role in LMS's rapid adjustment is uncertain.

We repeat the multi-perturbation regression of ΔSWV_{fast} vs ΔTCP_{fast} for each grid point in the latitude-pressure domain in Figures 3.18a-b. The ensemble average lapse rate tropopause is averaged over the last 10 years of the baseline fixed SST simulations. The correlation coefficient and slope (%/K) at each grid point in the pressure-latitude domain shows that the control of ΔTCP_{fast} over ΔSWV_{fast} follows the transport pattern of the BDC (Figs. 3.18a-b). The correlation coefficient and slope are large in the tropical overworld stratosphere and become weaker as one moves poleward and downward in the extra-tropics below 150 hPa. Vertical gradient in the slopes exist in the LMS region, decreasing toward the local tropopause. Again, this is consistent with the fact that water vapor in the LMS is controlled by several processes, not just TTL cold-point temperature.

The slope in Fig. 3.18b also has a hemispheric asymmetry, with larger values in the NH. This is due to the 10×BCperturbation, which heats the tropopause and LS more in the NH than the SH. If we remove 10×BCresults from the regression at each grid point (Figs. 3.18c-d), the hemispheric asymmetry in the slope disappears and the correlation coefficient in the NH LMS drops below 0.5. This indicates that the strength of the correlation may indicate not that ΔTCP_{fast} itself exerts control over the LMS ΔSWV_{fast}, but that other things that happen to correlate with the ΔTCP_{fast} do, such as convective transport into the LMS. Clearly, more work on this is warranted.

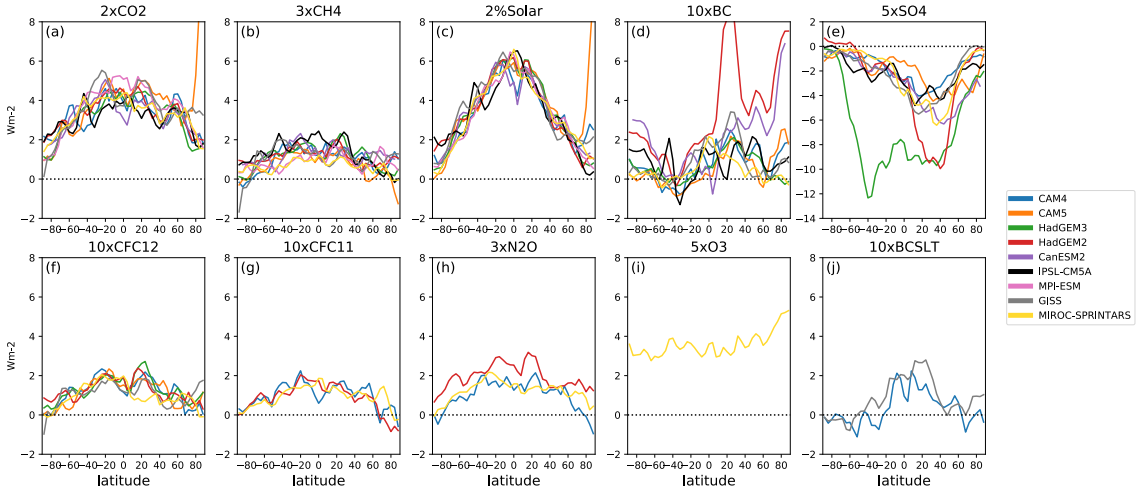

Figure 3.1: Zonal mean ERF (Wm^{-2}) at the top of atmosphere (TOA) from all models and perturbations investigated in this study. The colors indicate results from different models.

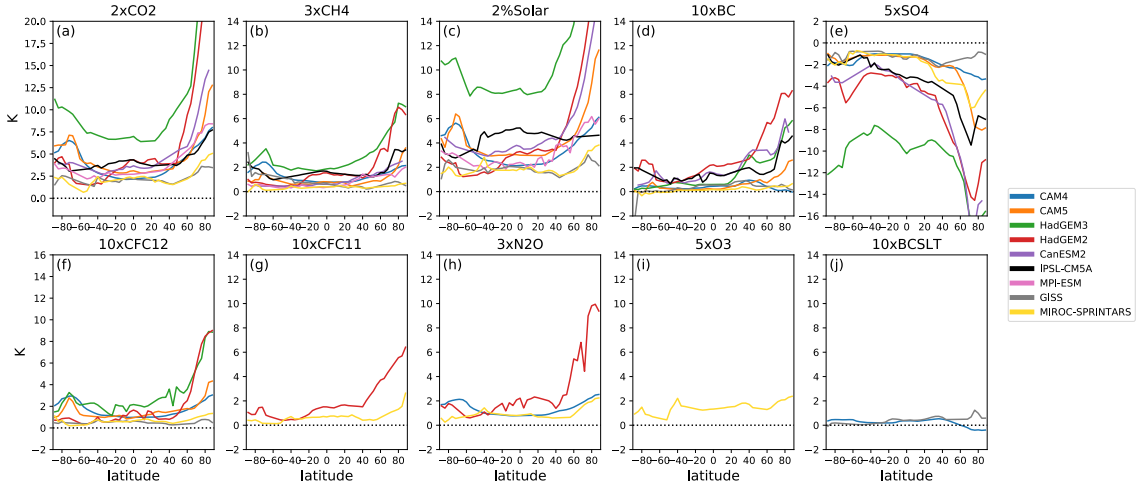

Figure 3.2: Zonal mean surface temperature change (K) at equilibrium from all models and perturbations investigated in this study. The colors indicate results from different models.

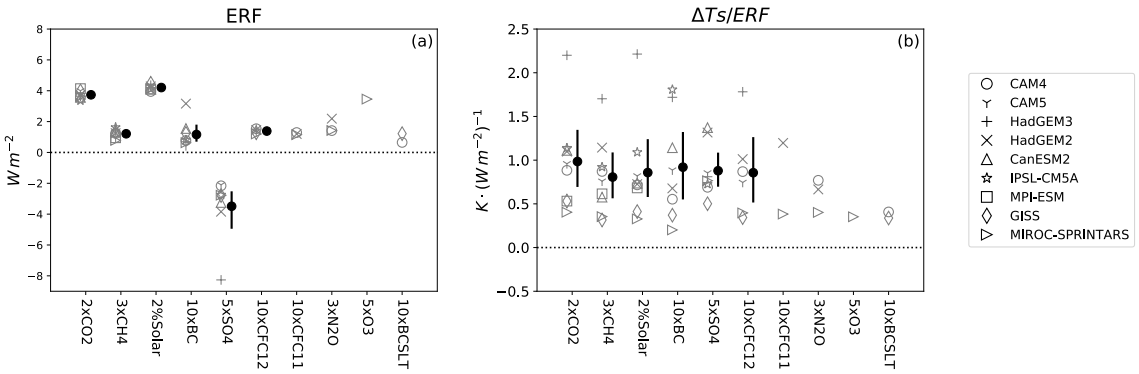

Figure 3.3: Panel (a): Global average ERF (Wm^{-2}) at the TOA. Panel (b): The global averaged surface temperature change at equilibrium per unit ERF ($K/(Wm^{-2})$). The marker shapes indicate results from different models. The solid circles and error bars for each perturbation plotted in weighted black are ensemble average and 2.5%-97.5% confidence intervals.

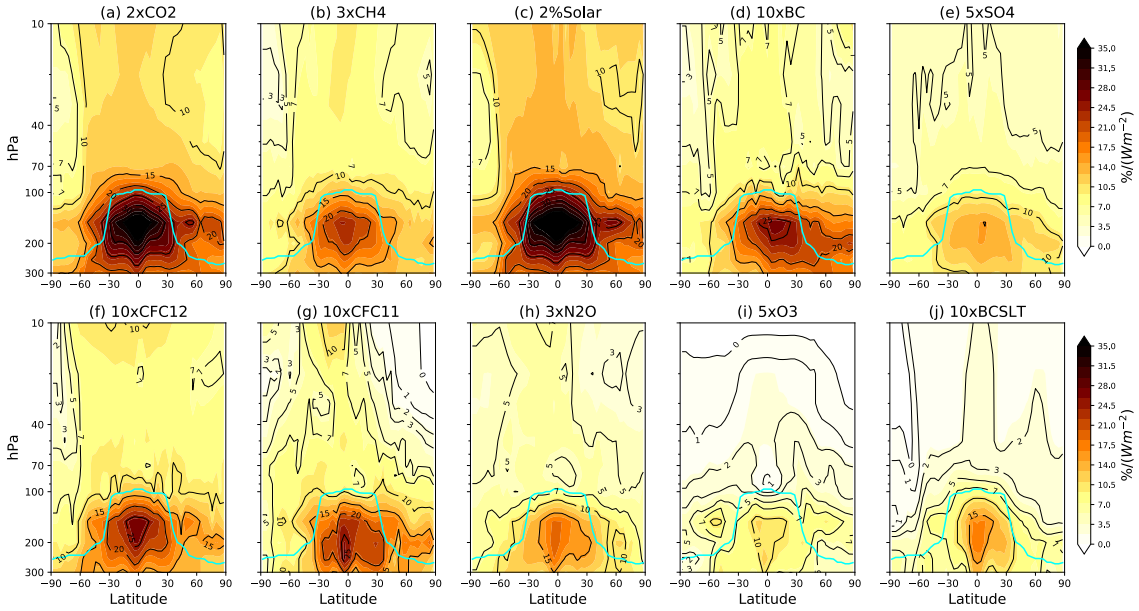

Figure 3.4: Zonal mean equilibrium $\Delta SWV_{slow}/ERF$. We show the percentage change relative to baseline ($\%/(Wm^{-2})$) in a latitude-pressure domain. For each perturbation, we show the ensemble average result. The solid line in cyan is the zonal mean lapse rate tropopause obtained from the coupled baseline simulation.

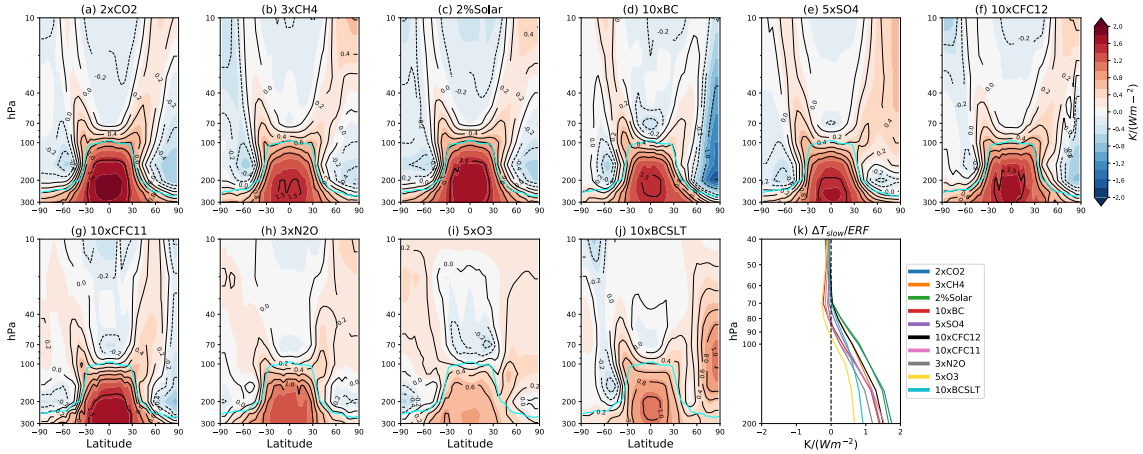

Figure 3.5: Panels (a)-(j): Zonal mean equilibrium $\Delta T_{slow}/ERF$ $(K/(Wm^{-2}))$ in a latitude-pressure domain. For each perturbation, we show the ensemble average result. The solid line in cyan is the zonal mean lapse rate tropopause obtained from the coupled baseline simulation. Panel (k): Profiles of ensemble average equilibrium $\Delta T_{slow}/ERF$ $(K/(Wm^{-2}))$ averaged between 30°N-30°S. Note the altitude range in this panel is between 200 and 40 hPa so that we can focus on the TTL. The color coding indicates results from different perturbations.

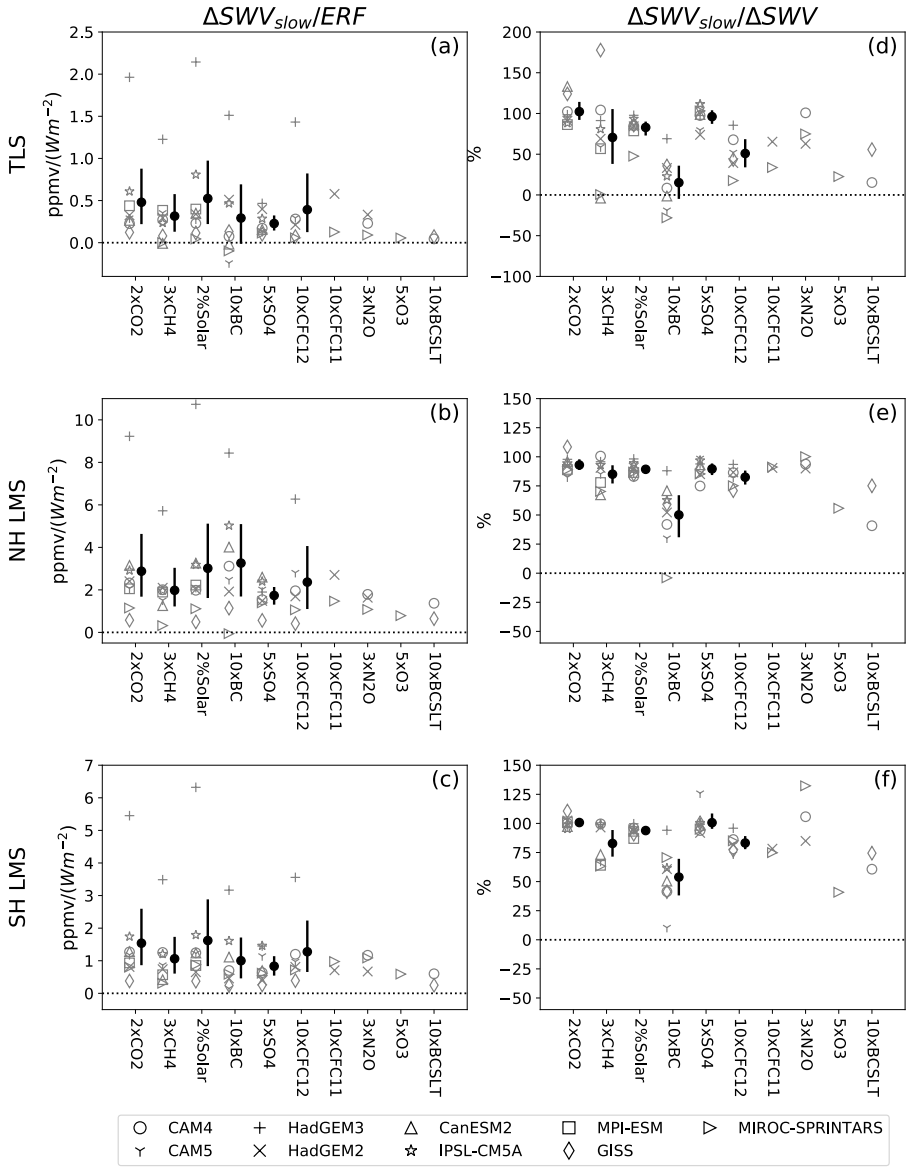

Figure 3.6: Panels (a)-(c): Equilibrium $\Delta SWV_{slow}/ERF$ $(ppmv/Wm^{-2})$ in tropical lower stratosphere at 70 hPa averaged between 30°N and 30°S, in the Northern Hemispheric lowermost stratosphere at 200 hPa averaged between 50°N and 90°N, and in the Southern Hemispheric lowermost stratosphere at 200 hPa averaged between 50°S and 90°S. Panels (d)-(f): Contribution (%) of equilibrium ΔSWV_{slow} to the total equilibrium ΔSWV. The marker shapes indicate results from different models. The solid circles and error bars for each perturbation plotted in weighted black are the ensemble average and 2.5%-97.5% confidence interval. Note that in the second column, we omit models with extremely small ΔSWV magnitudes that yield extremely large $\Delta SWV_{slow}/\Delta SWV$ ratios.

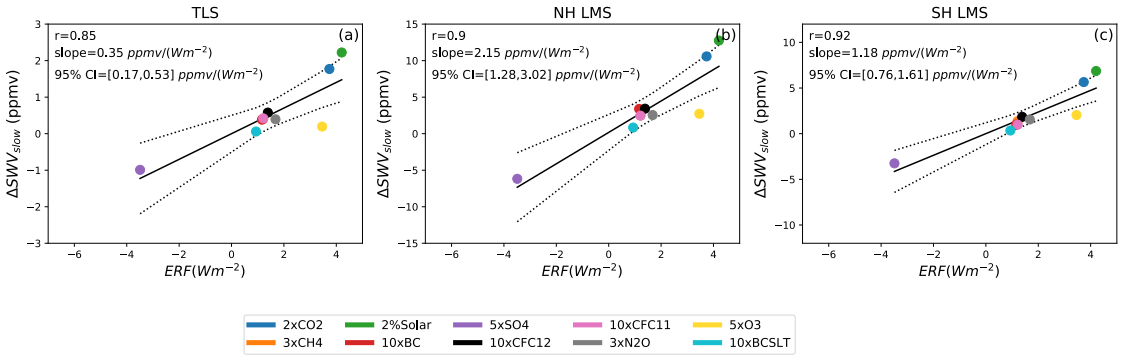

Figure 3.7: Linear regression between ensemble average equilibrium ΔSWV_{slow} (ppmv) and ensemble average ERF (Wm^{-2}) for all perturbations. The color coding indicates different perturbations. The black solid line is the linear fit of the regression. The black dotted lines indicate the linear fits within the 95% confidence interval, estimated using a t-test.

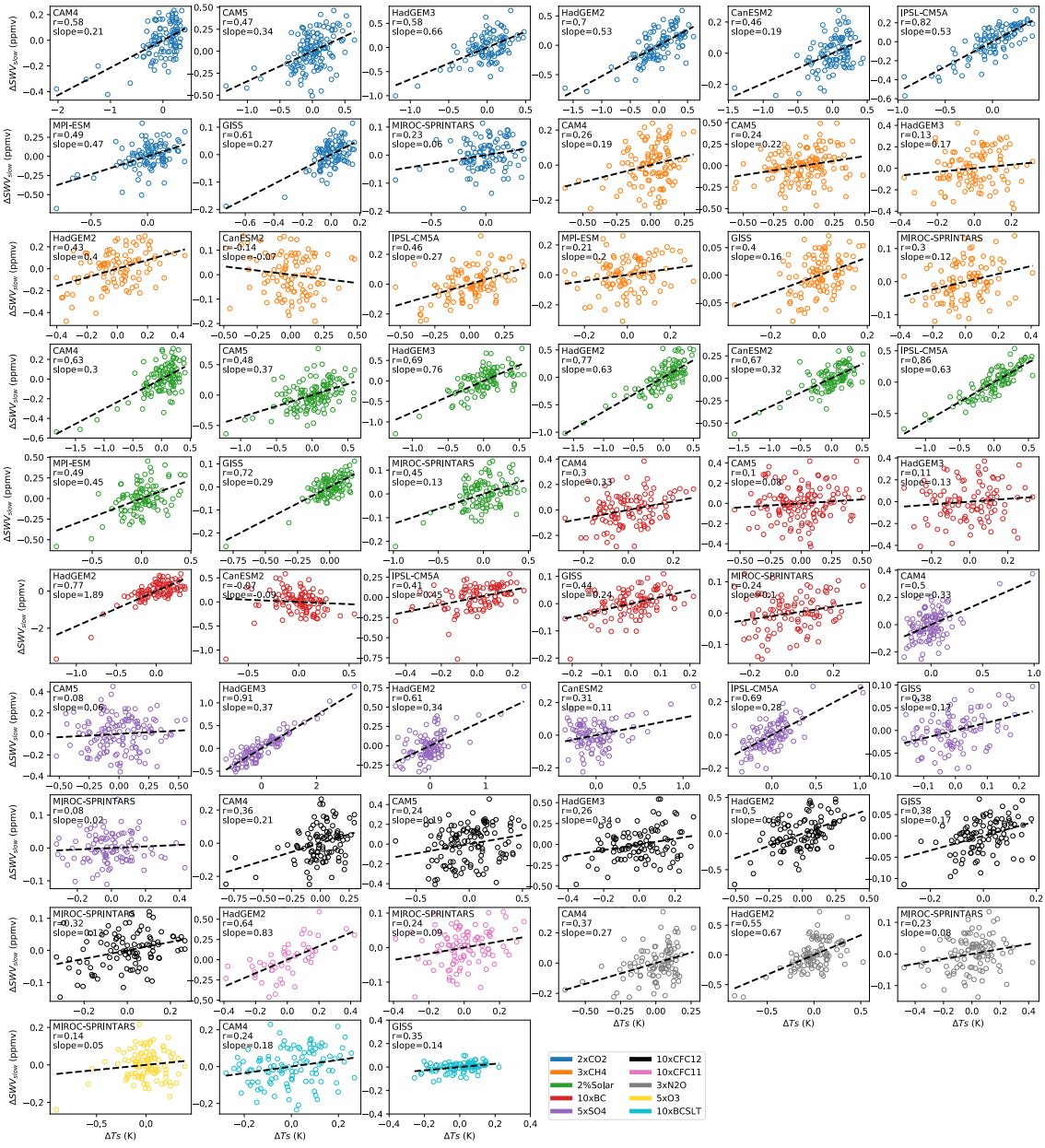

Figure 3.8: Linear regression between the annual mean ΔSWV_{slow} (ppmv) in the tropical lower stratosphere (70 hPa, 30°N - 30°S) and the annual mean global averaged surface temperature change, ΔTs (K), from the 100-year coupled model simulations. In each panel, the circles are annual mean results, and the dashed line is the linear fit. The color coding indicates results from different perturbations.

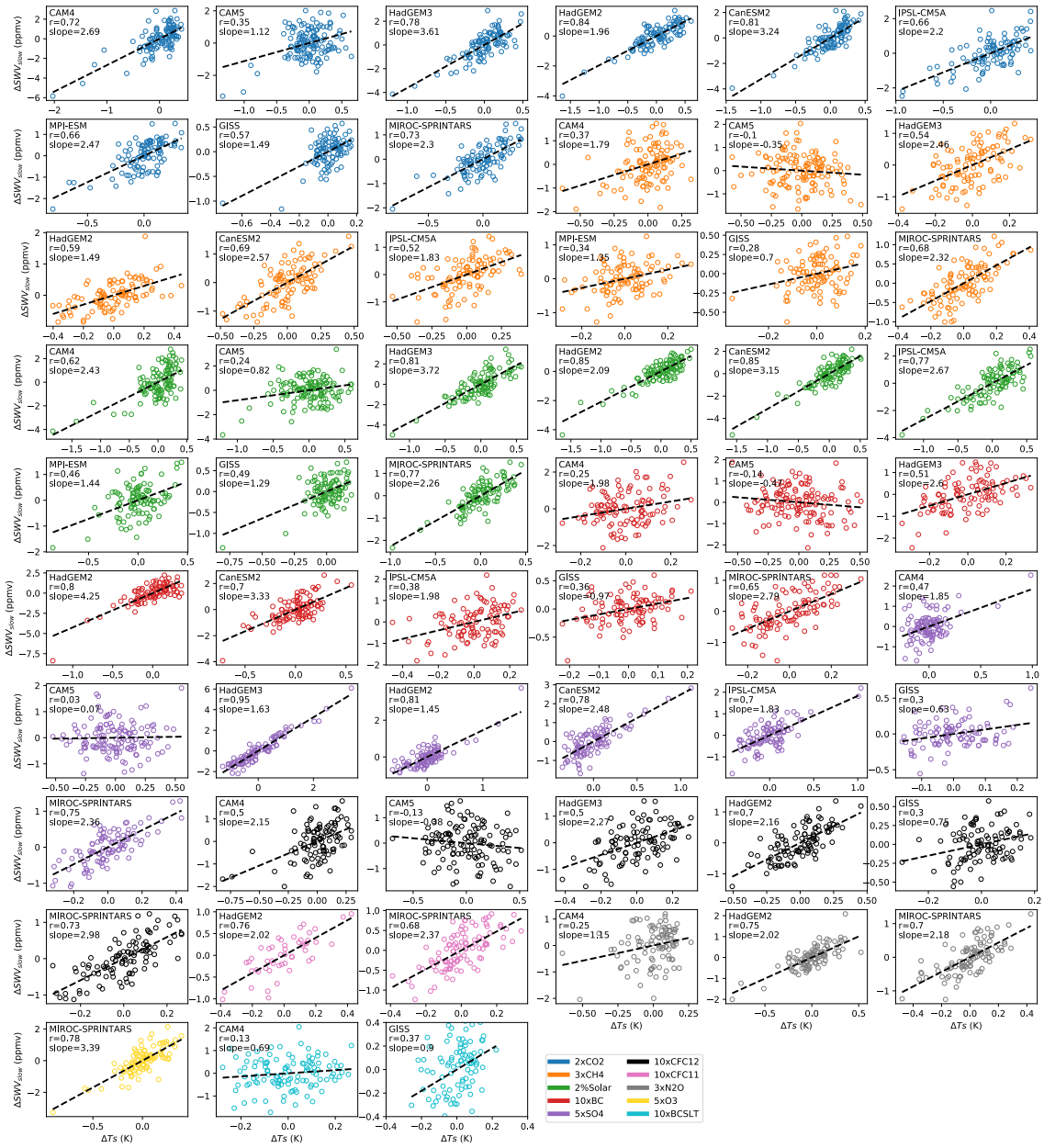

Figure 3.9: Same as Fig. 11, but for ΔSWV_{slow} (ppmv) in the Northern Hemispheric lowermost stratosphere (200 hPa, 50°N - 90°N).

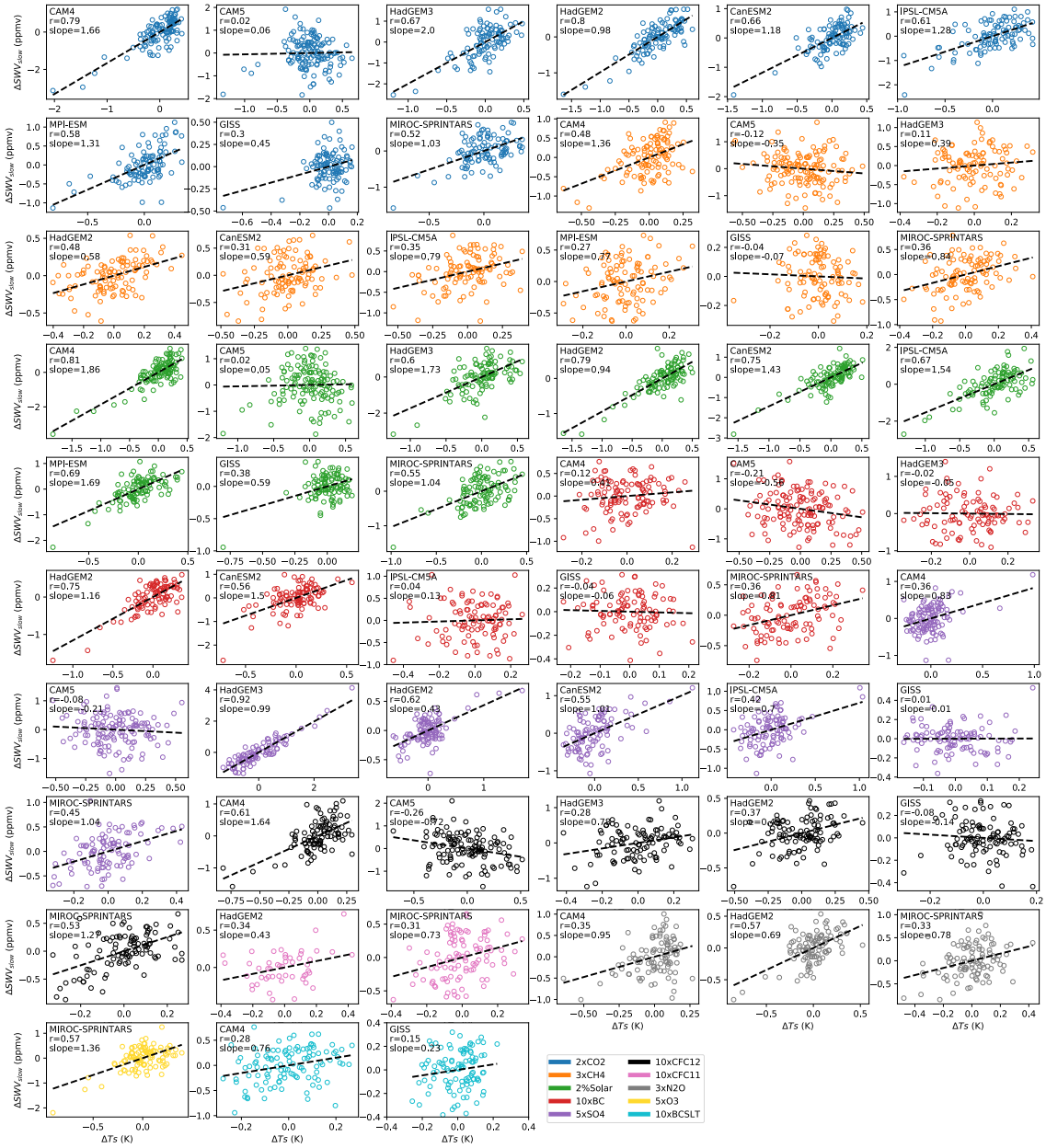

Figure 3.10: Same as Fig. 11, but for ΔSWV_{slow} (ppmv) in the Southern Hemispheric lowermost stratosphere (200 hPa, 50°S - 90°S).

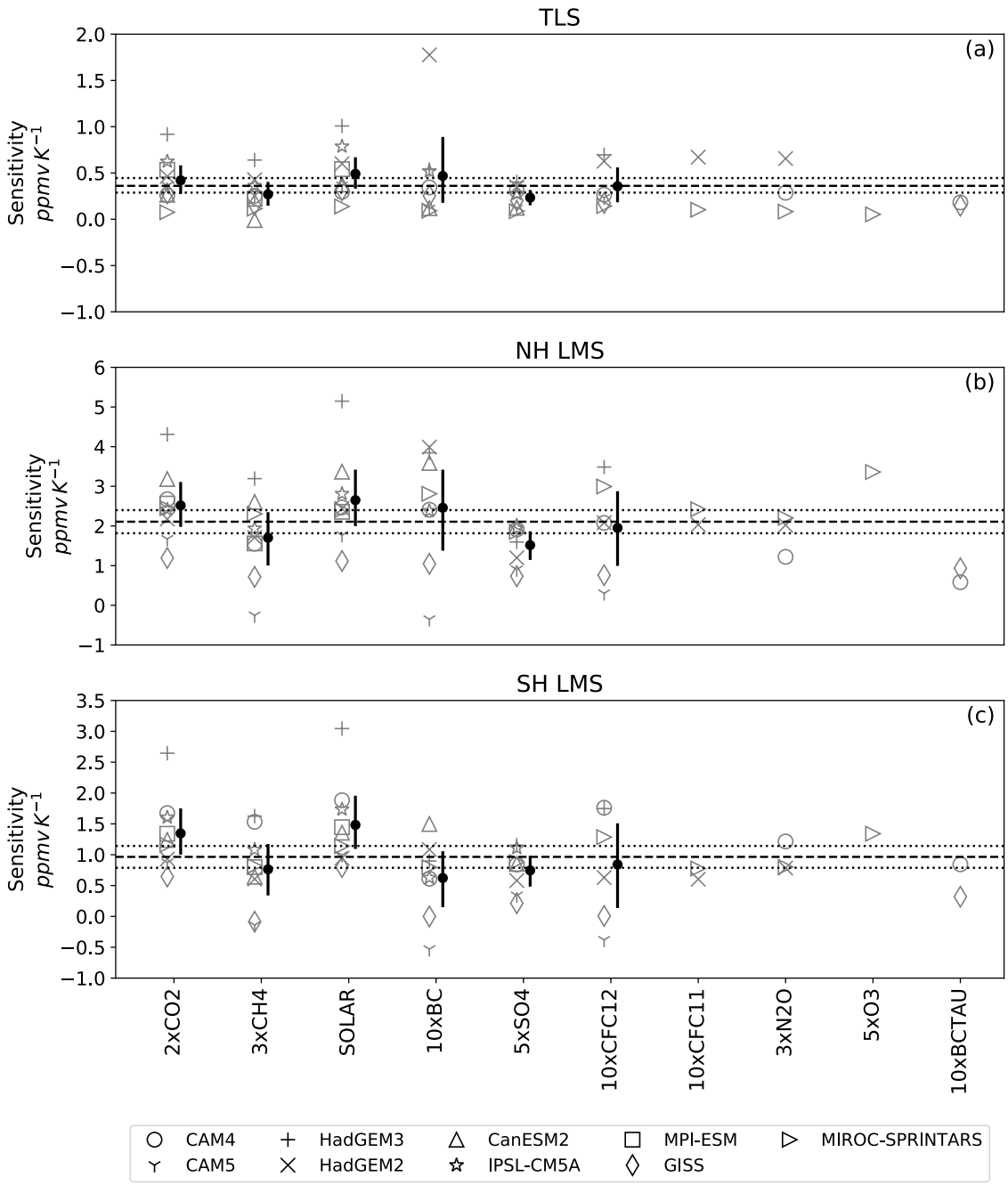

Figure 3.11: Slopes ($ppmvK^{-1}$) from the linear regression between annual mean ΔSWV_{slow} time series and annual mean ΔTs time series. The marker shapes indicate results from different models. The solid circles and error bars for each perturbation plotted in weighted black are ensemble average and 2.5%-97.5% confidence intervals. The horizontal dashed line and the horizontal dotted lines are ensemble average and 2.5%-97.5% confidence intervals for slopes from all models and perturbations.

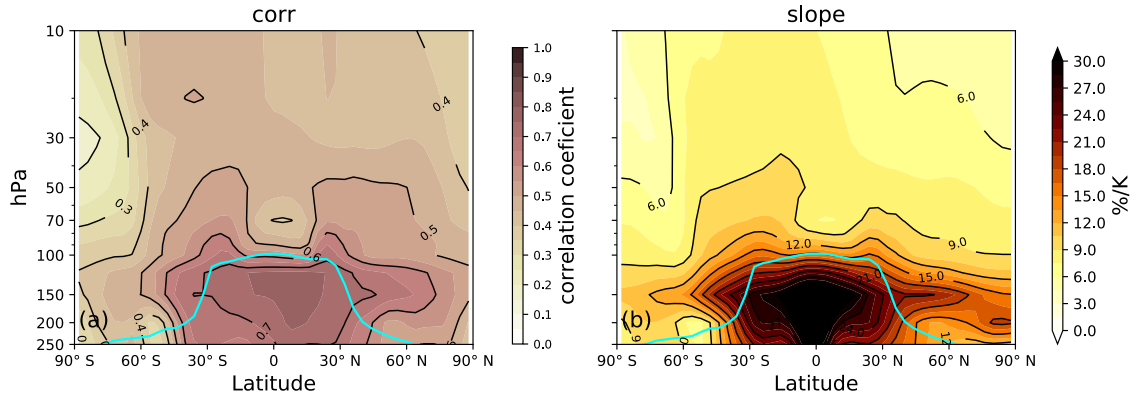

Figure 3.12: Ensemble and perturbation average correlation coefficient (Panel a) and slope $(\%/K)$ (Panel b) from the regression between annual mean time series of ΔSWV_{slow} at each latitude grid point and pressure level and annual mean time series of global average ΔTs. The solid cyan line is the ensemble and perturbation average lapse rate tropopause.

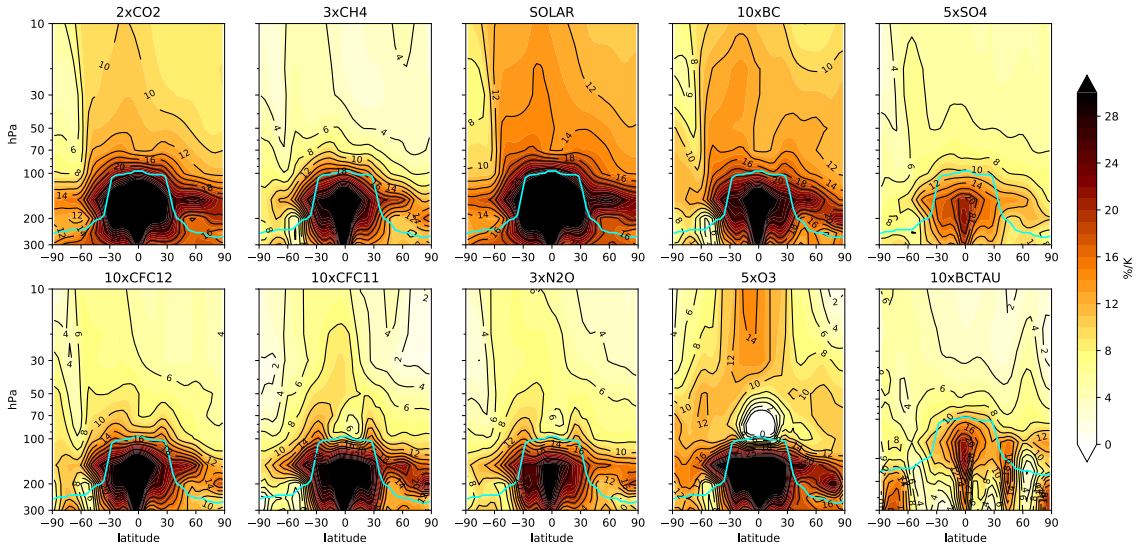

Figure 3.13: Ensemble average slope $(\%/K)$ for each individual perturbation from the regression between annual mean time series of ΔSWV_{slow} at each latitude grid point and pressure level and annual mean time series of global average ΔTs.

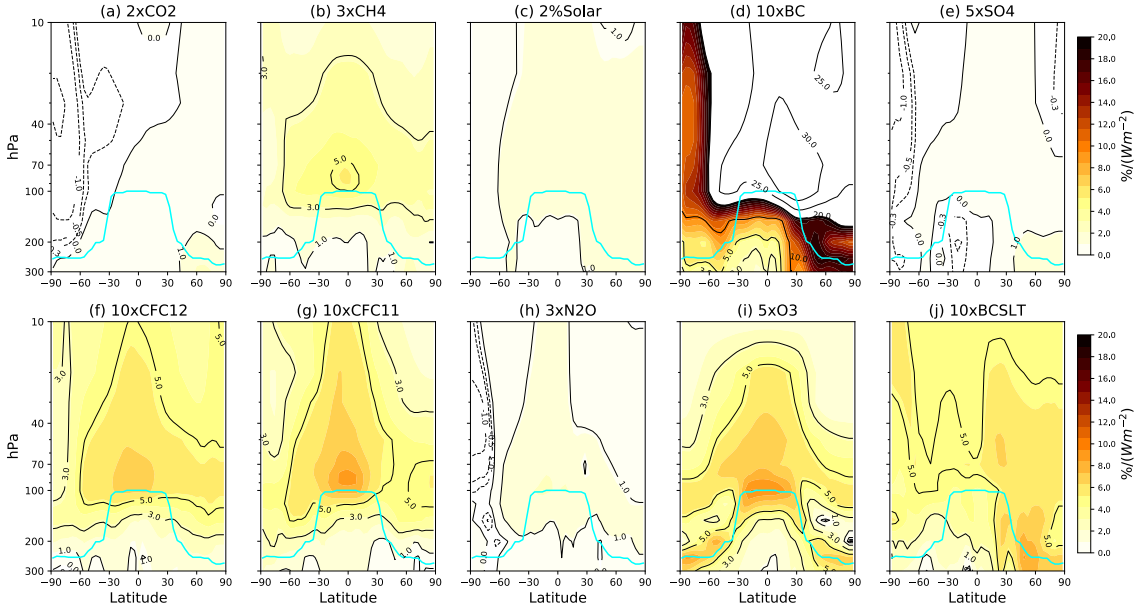

Figure 3.14: Zonal mean $\Delta SWV_{fast}/ERF$. We show the percentage change relative to baseline ($\%/(Wm^{-2})$) in a latitude-pressure domain. For each perturbation, we show the ensemble average result. The solid line in cyan is the zonal mean lapse rate tropopause obtained from the fixed SST baseline simulation averaged during the last 10 years.

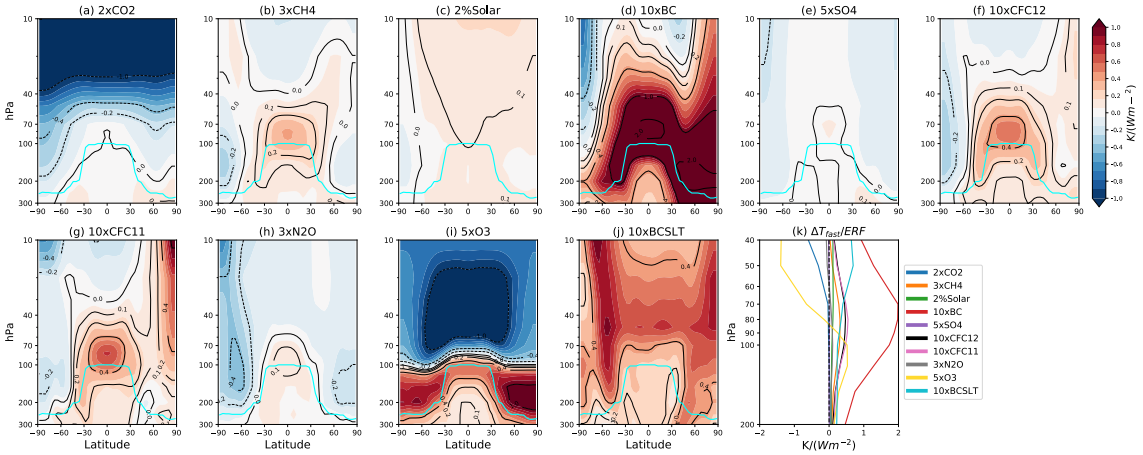

Figure 3.15: Same as Figure 8, but for $\Delta T_{fast}/ERF$ ($K/(Wm^{-2})$) and lapse rate tropopause obtained from the fixed SST baseline simulation averaged during the last 10 years.

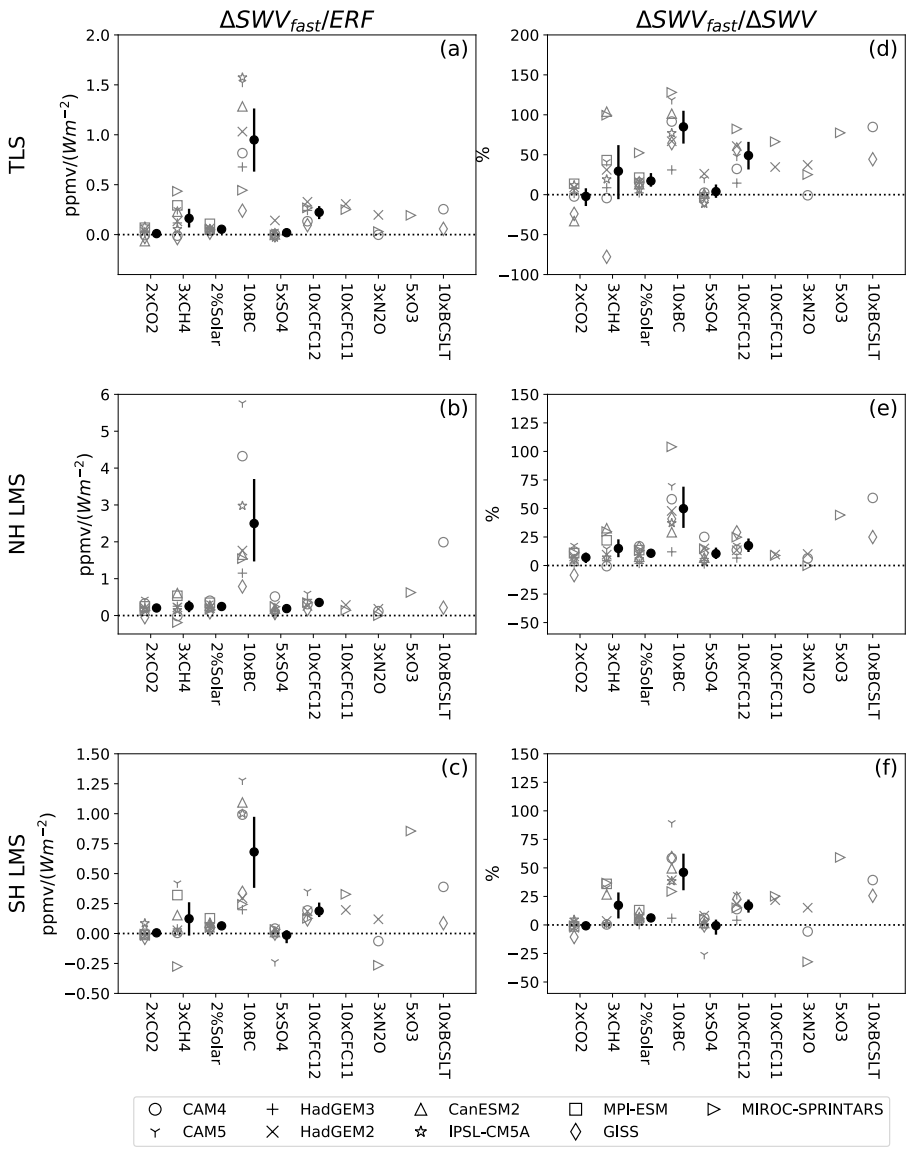

Figure 3.16: Same as Fig. 9, but for $\Delta SWV_{fast}/ERF$ $(ppmv/(Wm^{-2}))$ and the percentage contribution (%) of ΔSWV_{fast} to total equilibrium ΔSWV.

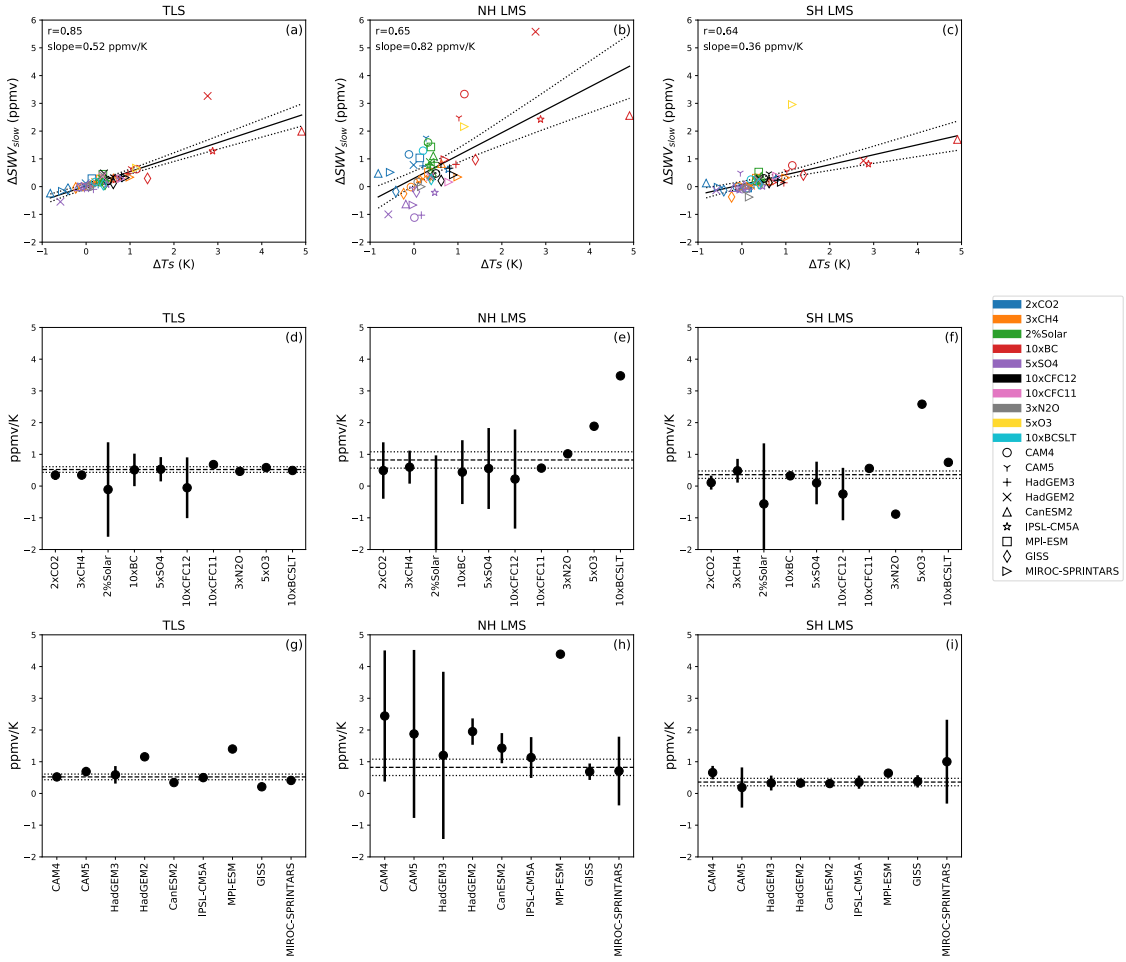

Figure 3.17: Panels (a)-(c): Linear regression between ΔSWV_{fast} (ppmv) and ΔTCP_{fast} (K) from all models and perturbations. The color coding indicates different perturbations, while the marker shapes indicate results from different models. The black solid line is the linear fit of the regression. The black dotted lines indicate the linear fits within the 95% confidence interval, estimated using a t-test. Panels (d)-(f): Slopes and their 95% confidence intervals obtained from linear regression between ΔSWV_{fast} (ppmv) and ΔTCP_{fast} (K) for each individual perturbation. Panels (g)-(i): Slopes and their 95% confidence intervals obtained from linear regression between ΔSWV_{fast} (ppmv) and ΔTCP_{fast} (K) for each individual model. The black dashed lines and dotted lines in panels (d)-(i) are the slopes and their 95% confidence intervals of regressions in (a)-(c).

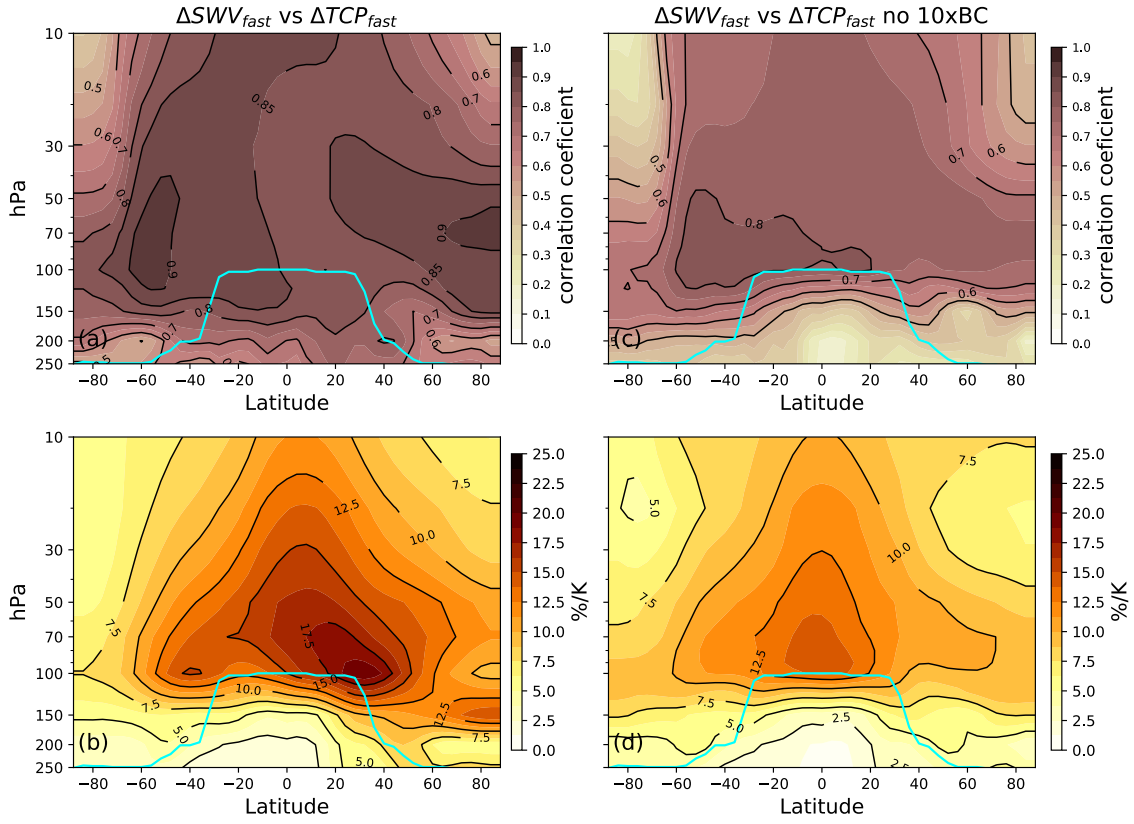

Figure 3.18: Panels (a)-(b): Correlation coefficient and slope from the regression between ΔSWV_{fast} (ppmv) and ΔTCP_{fast} (K) at each grid point in a pressure-latitude domain. The ensemble and perturbation average tropopause is averaged over the last 10 years of the fixed SST simulations. Panels (c)-(d): Same as (a)-(b), but we removed the 10×BCresults from the regression at each grid point.

4. SUMMARY AND CONCLUSIONS *

In this study, we investigated the response of stratospheric water vapor (SWV) in a range of different climate change mechanisms using a multi-model and multiple forcing agent framework. We use output from nine models participating the PDRMIP, which are models within CMIP5, each performing a baseline and up to 10 climate perturbation experiments, including 2×CO_2, 3×CH_4, 2%Solar, 10×BC, 5×SO_4, 10×CFC-11, 10×CFC-12, 3×N_2O, 5×O_3, and 10×BCSLT (Table 2.1). Each perturbation experiment and each baseline simulation are performed with two configurations, including a fixed SST simulation (at least 15 years) and a fully coupled simulation (at least 100 years).

It is of great interest for the climate community to understand how SWV changes when the climate changes, since SWV plays an important role in the Earth's radiative budget and stratospheric ozone chemistry (Solomon et al., 1986, 2010; Dvortsov and Solomon, 2001; Forster and Shine, 2002). Previous studies showed that, when greenhouse gases (GHGs) such as CO_2 increase, surface warming is the dominant cause of the long-term trend in SWV, which constitutes a climate feedback (Gettelman et al., 2010; Shu et al., 2011; Dessler et al., 2013; Revell et al., 2016; Yang et al., 2016; Lin et al., 2017; Smalley et al., 2017; Banerjee et al., 2019). It is not clear, however, whether forcing agents with different climate change mechanisms all affect SWV similarly.

To better understand the SWV response (ΔSWV), calculated as the change in SWV mixing ratio in the perturbed coupled run relative to that in the baseline coupled run, we partition it into two parts, the slow response (ΔSWV_{slow}) and the fast response (Δ-

*This dissertation is adapted with permission under the Creative Commons Attribution 4.0 License (https://creativecommons.org/licenses/by/4.0/) from "The response of stratospheric water vapor to climate change driven by different forcing agents" by Xun Wang and Andrew Dessler, 2020, preprinted in *Atmospheric Chemistry and Physics Discussion*, 2020, 1-22, Copyright [2020] by Copernicus Publications and the authors of the manuscript and its final journal article.

SWV_{fast}). The ΔSWV_{fast} occurs on shorter time scales, before the surface temperature changes. It is calculated as is the difference between the SWV mixing ratio in the fixed SST run with the forcing perturbation and that in the fixed SST run with the baseline atmosphere. The ΔSWV_{slow} occurs on longer time scales, which is coupled with the surface temperature change. To estimate the time series of ΔSWV_{slow}, we use annual mean ΔSWV over the entire coupled run period (at least 100 years) minus our estimate of ΔSWV_{fast}. To estimate the equilibrium ΔSWV_{slow}, we use a regression method discussed in Section 2.2 to first compute equilibrium ΔSWV, and then subtract ΔSWV_{fast} from it. When comparing magnitudes of ΔSWV_{slow} and ΔSWV_{fast}across different climate perturbations, we normalize the quantities by effective radiative forcing (ERF) at the top of atmosphere (TOA), so that differences in the ERF do not confound our results.

Our results show that, for most perturbations, the total equilibrium ΔSWV in the tropical lower stratosphere (TLS, 70 hPa, 30°S-30°N) and in the lowermost stratosphere (LMS, 200 hPa, 50°N-90°N and 50°S-90°S) mainly consists of ΔSWV_{slow} (Fig. 3.6). The zonal mean equilibrium ΔSWV_{slow} shows that there is an average moistening of 0.33$\pm$0.09 $ppmv/(Wm^{-2})$, equivalent to 7.80$\pm$2.00 $\%/(Wm^{-2})$, in the stratosphere for all the perturbations, with a larger response in the LMS (Fig.3.4).

The equilibrium ΔSWV_{slow}/ERF shows general agreement in the zonal mean pattern and magnitudes across different climate perturbations, which corresponds to the general agreement in the slow temperature response (Fig. 3.5). Specifically, a regression between the ensemble average equilibrium ΔSWV_{slow} and ERF shows that, water vapor increases by 0.35 $ppmv/(Wm^{-2})$ in the TLS, 2.15 $ppmv/(Wm^{-2})$ in the NH LMS, and 1.18 $ppmv/(Wm^{-2})$ in the SH LMS. These indicate that, for most climate perturbations, the slow response is forced by similar mechanisms. Moreover, our results agree with Richardson et al. (2019) that, the global average surface temperature responds to different forcing agents with a similar efficacy (Fig. 3.3). This leads to a discussion of the

relationship between ΔSWV_{slow} and surface temperature change across different climate perturbations.

Most perturbations and models show that the annual mean ΔSWV_{slow} time series is positively correlated with the annual mean time series of surface temperature change (ΔTs) (Figs. 3.8-3.10), and that the slopes of the linear fits fall within a close range across different perturbations (Fig. 3.11). This indicates that the surface temperature change contributes to the long-term trend in SWV not only when climate is perturbed by increased CO_2 (Gettelman et al., 2010; Shu et al., 2011; Dessler et al., 2013; Revell et al., 2016; Yang et al., 2016; Lin et al., 2017; Smalley et al., 2017; Banerjee et al., 2019), but also across a wider range of different climate change mechanisms.

Furthermore, the ΔSWV_{slow} time series responds to the ΔTs time series with a similar sensitivity across different climate change mechanisms. Specifically, the ensemble and perturbation average slope is 2.1 $ppmv\,K^{-1}$ in the NH, and 0.97 $ppmv\,K^{-1}$ in the SH, with 95% confidence intervals of 1.82-2.39 $ppmv\,K^{-1}$ and 0.79-1.15 $ppmv\,K^{-1}$, respectively. This relation can be extended to the entire stratosphere (Figs. 3.12 and 3.13). The ΔSWV_{slow} in the LMS has larger sensitivity to ΔTs compared to the tropical overworld, which reflects different transport pathways into the LMS compared to the overworld (Dessler et al., 1995; Holton et al., 1995; Plumb, 2002; Gettelman et al., 2011). The even larger sensitivity in the NH LMS is consistent with hemispheric asymmetries in the isentropic transport and convective moistening reported by previous studies (Pan et al., 1997, 2000; Dethof et al., 1999, 2000; Ploeger et al., 2013; Dessler and Sherwood, 2004; Smith et al., 2017; Ueyama et al., 2018; Wang et al., 2019).

The fast responses of SWV from most perturbations are weak and plays a smaller role (Fig. 3.16). Unlike the slow response, the fast responses from different perturbed simulations have distinct patterns and magnitudes (Figs. 3.14-3.16). For forcing agents that directly heat tropopause levels (Fig. 3.15), ΔSWV_{fast} makes a larger contribution to total

equilibrium ΔSWV. In particular, when climate is perturbed by 10×BC, the fast response dominates the total response and has a larger magnitude than any other perturbed simulations. Other forcing agents, including 10×CFC-11, 10×CFC-12, 3×CH_4, and 5×O_3 produce larger fast responses, due to TTL heating through longwave absorption in the atmospheric window range and shortwave absorption, but are not as strong as 10×BC.

We quantify the relationship between ΔSWV_{fast} and the fast adjustment of TTL temperatures across different climate change mechanisms. In the TLS, the ΔSWV_{fast} is positively correlated with the fast response of the cold point temperature across all models and perturbations (Fig. 3.17), with a slope of 0.52 $ppmv\,K^{-1}$, which is consistent with the Clausius-Clapeyron relationship evaluated near the tropical tropopause (Randel and Park, 2019). The control of cold point temperature fast response over ΔSWV_{fast} follows the transport pattern of the BDC, which is stronger in the overworld and becomes weaker at higher latitudes in the LMS below 150 hPa (Fig. 3.18). This means that in the LMS, the fast response of cold point temperature plays a smaller role in controlling the ΔSWV_{fast}, and that other factors are also needed to fully represent the LMS ΔSWV_{fast}.

REFERENCES

Adams, B. K. and Dessler, A. E. (2019). Estimating transient climate response in a large-ensemble global climate model simulation. *Geophysical Research Letters*, 46(1):311–317.

Anderson, J. G., Wilmouth, D. M., Smith, J. B., and Sayres, D. S. (2012). UV Dosage Levels in Summer: Increased Risk of Ozone Loss from Convectively Injected Water Vapor. *Science*, 337(6096):835–839.

Arora, V. K., Scinocca, J. F., Boer, G. J., Christian, J. R., Denman, K. L., Flato, G. M., Kharin, V. V., Lee, W. G., and Merryfield, W. J. (2011). Carbon emission limits required to satisfy future representative concentration pathways of greenhouse gases. *Geophysical Research Letters*, 38(5):n/a–n/a.

Banerjee, A., Chiodo, G., Previdi, M., Ponater, M., Conley, A. J., and Polvani, L. M. (2019). Stratospheric water vapor: an important climate feedback. *Climate Dynamics*.

Bellouin, N., Collins, W. J., Culverwell, I. D., Halloran, P. R., Hardiman, S. C., Hinton, T. J., Jones, C. D., McDonald, R. E., McLaren, A. J., O'Connor, F. M., Roberts, M. J., Rodriguez, J. M., Woodward, S., Best, M. J., Brooks, M. E., Brown, A. R., Butchart, N., Dearden, C., Derbyshire, S. H., Dharssi, I., Doutriaux-Boucher, M., Edwards, J. M., Falloon, P. D., Gedney, N., Gray, L. J., Hewitt, H. T., Hobson, M., Huddleston, M. R., Hughes, J., Ineson, S., Ingram, W. J., James, P. M., Johns, T. C., Johnson, C. E., Jones, A., Jones, C. P., Joshi, M. M., Keen, A. B., Liddicoat, S., Lock, A. P., Maidens, A. V., Manners, J. C., Milton, S. F., Rae, J. G. L., Ridley, J. K., Sellar, A., Senior, C. A., Totterdell, I. J., Verhoef, A., Vidale, P. L., and Wiltshire, A. (2011). The HadGEM2 family of Met Office Unified Model climate configurations. *Geoscientific Model Development*, 4(3):723–757.

Brasseur, G. P. and Solomon, S. (2005). *Aeronomy of the Middle Atmosphere*, volume 32 of *Atmospheric and Oceanographic Sciences Library*. Springer Netherlands, Dordrecht.

Brewer, A. W. (1949). Evidence for a world circulation provided by the measurements of helium and water vapour distribution in the stratosphere. *Quarterly Journal of the Royal Meteorological Society*, 75(326):351–363.

Chen, P. (1995). Isentropic cross-tropopause mass exchange in the extratropics. *Journal of Geophysical Research*, 100(D8):16661.

Collins, W. J., Bellouin, N., Doutriaux-Boucher, M., Gedney, N., Halloran, P., Hinton, T., Hughes, J., Jones, C. D., Joshi, M., Liddicoat, S., Martin, G., O'Connor, F., Rae, J., Senior, C., Sitch, S., Totterdell, I., Wiltshire, A., and Woodward, S. (2011). Development and evaluation of an Earth-System model HadGEM2. *Geoscientific Model Development*, 4(4):1051–1075.

Dessler, A. E. (2020). Potential Problems Measuring Climate Sensitivity from the Historical Record. *Journal of Climate*, 33(6):2237–2248.

Dessler, A. E., Hintsa, E. J., Weinstock, E. M., Anderson, J. G., and Chan, K. R. (1995). Mechanisms controlling water vapor in the lower stratosphere: A tale of two stratospheres. *Journal of Geophysical Research*, 100(D11):23167.

Dessler, A. E., Schoeberl, M. R., Wang, T., Davis, S. M., and Rosenlof, K. H. (2013). Stratospheric water vapor feedback. *Proceedings of the National Academy of Sciences*, 110(45):18087–18091.

Dessler, A. E. and Sherwood, S. C. (2004). Effect of convection on the summertime extratropical lower stratosphere. *Journal of Geophysical Research: Atmospheres*, 109(D23).

Dessler, A. E., Ye, H., Wang, T., Schoeberl, M. R., Oman, L. D., Douglass, A. R., Butler, A. H., Rosenlof, K. H., Davis, S. M., and Portmann, R. W. (2016). Transport of ice into the stratosphere and the humidification of the stratosphere over the 21st century. *Geophysical Research Letters*, 43(5):2323–2329.

Dessler, A. E. and Zelinka, M. D. (2015). *Encyclopedia of Atmospheric Sciences*. Climate Feedbacks. Academic Press, Oxford.

Dethof, A., O'Neill, A., and Slingo, J. (2000). Quantification of the isentropic mass transport across the dynamical tropopause. *Journal of Geophysical Research: Atmospheres*, 105(D10):12279–12293.

Dethof, A., O'Neill, A., Slingo, J. M., and Smit, H. G. J. (1999). A mechanism for moistening the lower stratosphere involving the Asian summer monsoon. *Quarterly Journal of the Royal Meteorological Society*, 125(556):1079–1106.

Dufresne, J.-L., Foujols, M.-A., Denvil, S., Caubel, A., Marti, O., Aumont, O., Balkanski, Y., Bekki, S., Bellenger, H., Benshila, R., Bony, S., Bopp, L., Braconnot, P., Brockmann, P., Cadule, P., Cheruy, F., Codron, F., Cozic, A., Cugnet, D., de Noblet, N., Duvel, J.-P., Ethé, C., Fairhead, L., Fichefet, T., Flavoni, S., Friedlingstein, P., Grandpeix, J.-Y., Guez, L., Guilyardi, E., Hauglustaine, D., Hourdin, F., Idelkadi, A., Ghattas, J., Joussaume, S., Kageyama, M., Krinner, G., Labetoulle, S., Lahellec, A., Lefebvre, M.-P., Lefevre, F., Levy, C., Li, Z. X., Lloyd, J., Lott, F., Madec, G., Mancip, M., Marchand, M., Masson, S., Meurdesoif, Y., Mignot, J., Musat, I., Parouty, S., Polcher, J., Rio, C., Schulz, M., Swingedouw, D., Szopa, S., Talandier, C., Terray, P., Viovy, N., and Vuichard, N. (2013). Climate change projections using the IPSL-CM5 Earth System Model: from CMIP3 to CMIP5. *Climate Dynamics*, 40(9-10):2123–2165.

Dvortsov, V. L. and Solomon, S. (2001). Response of the stratospheric temperatures and ozone to past and future increases in stratospheric humidity. *Journal of Geophysical Research: Atmospheres*, 106(D7):7505–7514.

Forster, P. M. d. F. and Shine, K. P. (2002). Assessing the climate impact of trends in stratospheric water vapor. *Geophysical Research Letters*, 29(6):10–1–10–4.

Friedman, A. R., Hwang, Y.-T., Chiang, J. C. H., and Frierson, D. M. W. (2013). Interhemispheric Temperature Asymmetry over the Twentieth Century and in Future Projections.

Journal of Climate, 26(15):5419–5433.

Fueglistaler, S., Bonazzola, M., Haynes, P., and Peter, T. (2005). Stratospheric water vapor predicted from the lagrangian temperature history of air entering the stratosphere in the tropics. *Journal of Geophysical Research: Atmospheres*, 110(D8).

Fueglistaler, S., Dessler, A. E., Dunkerton, T. J., Folkins, I., Fu, Q., and Mote, P. W. (2009). Tropical tropopause layer. *Review of Geophysics*, 47:1–31.

Gent, P. R., Danabasoglu, G., Donner, L. J., Holland, M. M., Hunke, E. C., Jayne, S. R., Lawrence, D. M., Neale, R. B., Rasch, P. J., Vertenstein, M., Worley, P. H., Yang, Z.-L., and Zhang, M. (2011). The Community Climate System Model Version 4. *Journal of Climate*, 24(19):4973–4991.

Geoffroy, O., Saint-Martin, D., Olivié, D. J. L., Voldoire, A., Bellon, G., and Tytéca, S. (2013). Transient Climate Response in a Two-Layer Energy-Balance Model. Part I: Analytical Solution and Parameter Calibration Using CMIP5 AOGCM Experiments. *Journal of Climate*, 26(6):1841–1857.

Gettelman, A., Hegglin, M. I., Son, S.-W., Kim, J., Fujiwara, M., Birner, T., Kremser, S., Rex, M., Añel, J. A., Akiyoshi, H., Austin, J., Bekki, S., Braesike, P., Brühl, C., Butchart, N., Chipperfield, M., Dameris, M., Dhomse, S., Garny, H., Hardiman, S. C., Jöckel, P., Kinnison, D. E., Lamarque, J. F., Mancini, E., Marchand, M., Michou, M., Morgenstern, O., Pawson, S., Pitari, G., Plummer, D., Pyle, J. A., Rozanov, E., Scinocca, J., Shepherd, T. G., Shibata, K., Smale, D., Teyssèdre, H., and Tian, W. (2010). Multimodel assessment of the upper troposphere and lower stratosphere: Tropics and global trends. *Journal of Geophysical Research*, 115:D00M08.

Gettelman, A., Hoor, P., Pan, L. L., Randel, W. J., Hegglin, M. I., and Birner, T. (2011). THE EXTRATROPICAL UPPER TROPOSPHERE AND LOWER STRATOSPHERE. *Reviews of Geophysics*, 49(3):RG3003.

Giorgetta, M. A., Jungclaus, J., Reick, C. H., Legutke, S., Bader, J., Böttinger, M.,

Brovkin, V., Crueger, T., Esch, M., Fieg, K., Glushak, K., Gayler, V., Haak, H., Hollweg, H.-D., Ilyina, T., Kinne, S., Kornblueh, L., Matei, D., Mauritsen, T., Mikolajewicz, U., Mueller, W., Notz, D., Pithan, F., Raddatz, T., Rast, S., Redler, R., Roeckner, E., Schmidt, H., Schnur, R., Segschneider, J., Six, K. D., Stockhause, M., Timmreck, C., Wegner, J., Widmann, H., Wieners, K.-H., Claussen, M., Marotzke, J., and Stevens, B. (2013). Climate and carbon cycle changes from 1850 to 2100 in MPI-ESM simulations for the Coupled Model Intercomparison Project phase 5. *Journal of Advances in Modeling Earth Systems*, 5(3):572–597.

Gregory, J. M. (2004). A new method for diagnosing radiative forcing and climate sensitivity. *Geophysical Research Letters*, 31(3):L03205.

Guo, A., Moore, J. C., and Ji, D. (2018). Tropical atmospheric circulation response to the G1 sunshade geoengineering radiative forcing experiment. *Atmospheric Chemistry and Physics*, 18(12):8689–8706.

Hanisco, T. F., Moyer, E. J., Weinstock, E. M., St. Clair, J. M., Sayres, D. S., Smith, J. B., Lockwood, R., Anderson, J. G., Dessler, A. E., Keutsch, F. N., Spackman, J. R., Read, W. G., and Bui, T. P. (2007). Observations of deep convective influence on stratospheric water vapor and its isotopic composition. *Geophysical Research Letters*, 34(4):L04814.

Hansen, J., Sato, M., and Ruedy, R. (1997). Radiative forcing and climate response. *Journal of Geophysical Research: Atmospheres*, 102(D6):6831–6864.

Hassim, M. E. E. and Lane, T. P. (2010). A model study on the influence of overshooting convection on TTL water vapour. *Atmospheric Chemistry and Physics*, 10(20):9833–9849.

Haynes, P. and Shuckburgh, E. (2000). Effective diffusivity as a diagnostic of atmospheric transport: 2. Troposphere and lower stratosphere. *Journal of Geophysical Research: Atmospheres*, 105(D18):22795–22810.

Hegglin, M. I., Plummer, D. A., Shepherd, T. G., Scinocca, J. F., Anderson, J., Froidevaux,

L., Funke, B., Hurst, D., Rozanov, A., Urban, J., von Clarmann, T., Walker, K. A., Wang, H. J., Tegtmeier, S., and Weigel, K. (2014). Vertical structure of stratospheric water vapour trends derived from merged satellite data. *Nature Geoscience*, 7(10):768–776.

Hoffmann, L., Kaufmann, M., Spang, R., Müller, R., Remedios, J. J., Moore, D. P., Volk, C. M., von Clarmann, T., and Riese, M. (2008). Envisat MIPAS measurements of CFC-11: retrieval, validation, and climatology. *Atmospheric Chemistry and Physics*, 8(13):3671–3688.

Holton, J. R., Haynes, P. H., McIntyre, M. E., Douglass, A. R., Rood, R. B., and Pfister, L. (1995). Stratosphere-troposphere exchange. *Reviews of Geophysics*, 33(4):403.

Hoskins, B. J. (1991). Towards a PV-θ view of the general circulation. *Tellus A: Dynamic Meteorology and Oceanography*, 43(4):27–36.

Huang, Y., Zhang, M., Xia, Y., Hu, Y., and Son, S.-W. (2016). Is there a stratospheric radiative feedback in global warming simulations? *Climate Dynamics*, 46(1-2):177–186.

Hurrell, J. W., Holland, M. M., Gent, P. R., Ghan, S., Kay, J. E., Kushner, P. J., Lamarque, J.-F., Large, W. G., Lawrence, D., Lindsay, K., Lipscomb, W. H., Long, M. C., Mahowald, N., Marsh, D. R., Neale, R. B., Rasch, P., Vavrus, S., Vertenstein, M., Bader, D., Collins, W. D., Hack, J. J., Kiehl, J., and Marshall, S. (2013). The Community Earth System Model: A Framework for Collaborative Research. *Bulletin of the American Meteorological Society*, 94(9):1339–1360.

Jain, A. K., Briegleb, B. P., Minschwaner, K., and Wuebbles, D. J. (2000). Radiative forcings and global warming potentials of 39 greenhouse gases. *Journal of Geophysical Research: Atmospheres*, 105(D16):20773–20790.

Kay, J. E., Deser, C., Phillips, A., Mai, A., Hannay, C., Strand, G., Arblaster, J. M., Bates, S. C., Danabasoglu, G., Edwards, J., Holland, M., Kushner, P., Lamarque, J.-F., Lawrence, D., Lindsay, K., Middleton, A., Munoz, E., Neale, R., Oleson, K., Polvani,

L., and Vertenstein, M. (2015). The Community Earth System Model (CESM) Large Ensemble Project: A Community Resource for Studying Climate Change in the Presence of Internal Climate Variability. *Bulletin of the American Meteorological Society*, 96(8):1333–1349.

Kellmann, S., von Clarmann, T., Stiller, G. P., Eckert, E., Glatthor, N., Höpfner, M., Kiefer, M., Orphal, J., Funke, B., Grabowski, U., Linden, A., Dutton, G. S., and Elkins, J. W. (2012). Global CFC-11 (CCl 3 F) and CFC-12 (CCl 2 F 2) measurements with the Michelson Interferometer for Passive Atmospheric Sounding (MIPAS): retrieval, climatologies and trends. *Atmospheric Chemistry and Physics*, 12(24):11857–11875.

Lane, T. P. and Sharman, R. D. (2006). Gravity wave breaking, secondary wave generation, and mixing above deep convection in a three-dimensional cloud model. *Geophysical Research Letters*, 33(23):L23813.

Lin, P., Paynter, D., Ming, Y., and Ramaswamy, V. (2017). Changes of the Tropical Tropopause Layer under Global Warming. *Journal of Climate*, 30(4):1245–1258.

MacIntosh, C. R., Allan, R. P., Baker, L. H., Bellouin, N., Collins, W., Mousavi, Z., and Shine, K. P. (2016). Contrasting fast precipitation responses to tropospheric and stratospheric ozone forcing. *Geophysical Research Letters*, 43(3):1263–1271.

Maher, N., Milinski, S., Suarez-Gutierrez, L., Botzet, M., Dobrynin, M., Kornblueh, L., Kröger, J., Takano, Y., Ghosh, R., Hedemann, C., Li, C., Li, H., Manzini, E., Notz, D., Putrasahan, D., Boysen, L., Claussen, M., Ilyina, T., Olonscheck, D., Raddatz, T., Stevens, B., and Marotzke, J. (2019). The max planck institute grand ensemble: Enabling the exploration of climate system variability. *Journal of Advances in Modeling Earth Systems*, 11(7):2050–2069.

Manabe, S. and Wetherald, R. T. (1975). The Effects of Doubling the CO 2 Concentration on the climate of a General Circulation Model. *Journal of the Atmospheric Sciences*, 32(1):3–15.

Martin, T. H. D. T. G. M., Bellouin, N., Collins, W. J., Culverwell, I. D., Halloran, P. R., Hardiman, S. C., Hinton, T. J., Jones, C. D., McDonald, R. E., McLaren, A. J., O'Connor, F. M., Roberts, M. J., Rodriguez, J. M., Woodward, S., Best, M. J., Brooks, M. E., Brown, A. R., Butchart, N., Dearden, C., Derbyshire, S. H., Dharssi, I., Doutriaux-Boucher, M., Edwards, J. M., Falloon, P. D., Gedney, N., Gray, L. J., Hewitt, H. T., Hobson, M., Huddleston, M. R., Hughes, J., Ineson, S., Ingram, W. J., James, P. M., Johns, T. C., Johnson, C. E., Jones, A., Jones, C. P., Joshi, M. M., Keen, A. B., Liddicoat, S., Lock, A. P., Maidens, A. V., Manners, J. C., Milton, S. F., Rae, J. G. L., Ridley, J. K., Sellar, A., Senior, C. A., Totterdell, I. J., Verhoef, A., Vidale, P. L., and Wiltshire, A. (2011). The hadgem2 family of met office unified model climate configurations. *Geoscientific Model Development*, 4(3):723–757.

Maycock, A. C., Joshi, M. M., Shine, K. P., and Scaife, A. A. (2013). The Circulation Response to Idealized Changes in Stratospheric Water Vapor. *Journal of Climate*, 26(2):545–561.

Mote, P. W., Rosenlof, K. H., McIntyre, M. E., Carr, E. S., Gille, J. C., Holton, J. R., Kinnersley, J. S., Pumphrey, H. C., Russell III, J. M., and Waters, J. W. (1996). An atmospheric tape recorder: The imprint of tropical tropopause temperatures on stratospheric water vapor. *Journal of Geophysical Research*, 101(D2):3989–4006.

Mote, P. W., Rosenloh, K. H., Holton, J. R., Harwood, R. S., and Waters, J. W. (1995). Seasonal variations of water vapor in the tropical lower stratosphere. *Geophysical Research Letters*, 22(9):1093–1096.

Mullendore, G. L., Homann, A. J., Bevers, K., and Schumacher, C. (2009). Radar reflectivity as a proxy for convective mass transport. *Journal of Geophysical Research*, 114(D16):D16103.

Myhre, G., Forster, P. M., Samset, B. H., Hodnebrog, Ø., Sillmann, J., Aalbergsjø, S. G., Andrews, T., Boucher, O., Faluvegi, G., Fläschner, D., Iversen, T., Kasoar, M., Kharin,

V., Kirkevåg, A., Lamarque, J.-F., Olivié, D., Richardson, T. B., Shindell, D., Shine, K. P., Stjern, C. W., Takemura, T., Voulgarakis, A., and Zwiers, F. (2017). PDRMIP: A Precipitation Driver and Response Model Intercomparison ProjectProtocol and Preliminary Results. *Bulletin of the American Meteorological Society*, 98(6):1185–1198.

Myhre, G., Samset, B. H., Schulz, M., Balkanski, Y., Bauer, S., Berntsen, T. K., Bian, H., Bellouin, N., Chin, M., Diehl, T., Easter, R. C., Feichter, J., Ghan, S. J., Hauglustaine, D., Iversen, T., Kinne, S., Kirkevåg, A., Lamarque, J.-F., Lin, G., Liu, X., Lund, M. T., Luo, G., Ma, X., van Noije, T., Penner, J. E., Rasch, P. J., Ruiz, A., Seland, Ø., Skeie, R. B., Stier, P., Takemura, T., Tsigaridis, K., Wang, P., Wang, Z., Xu, L., Yu, H., Yu, F., Yoon, J.-H., Zhang, K., Zhang, H., and Zhou, C. (2013). Radiative forcing of the direct aerosol effect from AeroCom Phase II simulations. *Atmospheric Chemistry and Physics*, 13(4):1853–1877.

Neale, R. B., Richter, J. H., Conley, A. J., Park, S., Lauritzen, P. H., Gettelman, A., Williamson, D. L., Rasch, P. J., Vavrus, S. J., Taylor, M. A., Collins, W. D., Zhang, M., and Lin, S. (2010). Description of the NCAR Community Atmosphere Model (CAM 4.0). NCAR Technical Note NCAR/TN-485+STR, Climate And Global Dynamics Division, National Center For Atmospheric Research, Boulder, Colorado, USA.

Otto-Bliesner, B. L., Brady, E. C., Fasullo, J., Jahn, A., Landrum, L., Stevenson, S., Rosenbloom, N., Mai, A., and Strand, G. (2016). Climate Variability and Change since 850 CE: An Ensemble Approach with the Community Earth System Model. *Bulletin of the American Meteorological Society*, 97(5):735–754.

Pan, L., Solomon, S., Randel, W., Lamarque, J.-F., Hess, P., Gille, J., Chiou, E.-W., and McCormick, M. P. (1997). Hemispheric asymmetries and seasonal variations of the lowermost stratospheric water vapor and ozone derived from SAGE II data. *Journal of Geophysical Research: Atmospheres*, 102(D23):28177–28184.

Pan, L. L., Hintsa, E. J., Stone, E. M., Weinstock, E. M., and Randel, W. J. (2000). The

seasonal cycle of water vapor and saturation vapor mixing ratio in the extratropical lowermost stratosphere. *Journal of Geophysical Research: Atmospheres*, 105(D21):26519–26530.

Payan, S., Camy-Peyret, C., Oelhaf, H., Wetzel, G., Maucher, G., Keim, C., Pirre, M., Huret, N., Engel, A., Volk, M. C., Kuellmann, H., Kuttippurath, J., Cortesi, U., Bianchini, G., Mencaraglia, F., Raspollini, P., Redaelli, G., Vigouroux, C., De Mazière, M., Mikuteit, S., Blumenstock, T., Velazco, V., Notholt, J., Mahieu, E., Duchatelet, P., Smale, D., Wood, S., Jones, N., Piccolo, C., Payne, V., Bracher, A., Glatthor, N., Stiller, G., Grunow, K., Jeseck, P., Te, Y., and Butz, A. (2009). Validation of version-4.61 methane and nitrous oxide observed by MIPAS. *Atmospheric Chemistry and Physics*, 9(2):413–442.

Ploeger, F., Günther, G., Konopka, P., Fueglistaler, S., Müller, R., Hoppe, C., Kunz, A., Spang, R., Grooß, J.-U., and Riese, M. (2013). Horizontal water vapor transport in the lower stratosphere from subtropics to high latitudes during boreal summer. *Journal of Geophysical Research: Atmospheres*, 118(14):8111–8127.

Plumb, R. A. (2002). Stratospheric Transport. *Journal of the Meteorological Society of Japan. Ser. II*, 80(4B):793–809.

Ramanathan, V. (2001). Aerosols, Climate, and the Hydrological Cycle. *Science*, 294(5549):2119–2124.

Ramanathan, V. and Carmichael, G. (2008). Global and regional climate changes due to black carbon. *Nature Geoscience*, 1(4):221–227.

Randel, W. and Park, M. (2019). Diagnosing Observed Stratospheric Water Vapor Relationships to the Cold Point Tropical Tropopause. *Journal of Geophysical Research: Atmospheres*, page 2019JD030648.

Ray, E. A. (2004). Evidence of the effect of summertime midlatitude convection on the subtropical lower stratosphere from CRYSTAL-FACE tracer measurements. *Journal of*

Geophysical Research, 109(D18):D18304.

Revell, L. E., Stenke, A., Rozanov, E., Ball, W., Lossow, S., and Peter, T. (2016). The role of methane in projections of 21st century stratospheric water vapour. *Atmospheric Chemistry and Physics*, 16(20):13067–13080.

Richard, E. C. (2003). Large-scale equatorward transport of ozone in the subtropical lower stratosphere. *Journal of Geophysical Research*, 108(D23):4714.

Richardson, T. B., Forster, P. M., Smith, C. J., Maycock, A. C., Wood, T., Andrews, T., Boucher, O., Faluvegi, G., Fläschner, D., Hodnebrog, Ø., Kasoar, M., Kirkevåg, A., Lamarque, J., Mülmenstädt, J., Myhre, G., Olivié, D., Portmann, R. W., Samset, B. H., Shawki, D., Shindell, D., Stier, P., Takemura, T., Voulgarakis, A., and WatsonParris, D. (2019). Efficacy of Climate Forcings in PDRMIP Models. *Journal of Geophysical Research: Atmospheres*, 124(23):12824–12844.

Rind, D. (2008). The Consequences of Not Knowing Low- and High-Latitude Climate Sensitivity. *Bulletin of the American Meteorological Society*, 89(6):855–864.

Samset, B. H., Myhre, G., Forster, P. M., Hodnebrog, Ø., Andrews, T., Faluvegi, G., Fläschner, D., Kasoar, M., Kharin, V., Kirkevåg, A., Lamarque, J., Olivié, D., Richardson, T., Shindell, D., Shine, K. P., Takemura, T., and Voulgarakis, A. (2016). Fast and slow precipitation responses to individual climate forcers: A PDRMIP multimodel study. *Geophysical Research Letters*, 43(6):2782–2791.

Schmidt, G. A., Kelley, M., Nazarenko, L., Ruedy, R., Russell, G. L., Aleinov, I., Bauer, M., Bauer, S. E., Bhat, M. K., Bleck, R., Canuto, V., Chen, Y.-H., Cheng, Y., Clune, T. L., Del Genio, A., de Fainchtein, R., Faluvegi, G., Hansen, J. E., Healy, R. J., Kiang, N. Y., Koch, D., Lacis, A. A., LeGrande, A. N., Lerner, J., Lo, K. K., Matthews, E. E., Menon, S., Miller, R. L., Oinas, V., Oloso, A. O., Perlwitz, J. P., Puma, M. J., Putman, W. M., Rind, D., Romanou, A., Sato, M., Shindell, D. T., Sun, S., Syed, R. A., Tausnev, N., Tsigaridis, K., Unger, N., Voulgarakis, A., Yao, M.-S., and Zhang, J. (2014). Con-

figuration and assessment of the GISS ModelE2 contributions to the CMIP5 archive. *Journal of Advances in Modeling Earth Systems*, 6(1):141–184.

Schoeberl, M. R., Douglass, A. R., Newman, P. A., Lait, L. R., Lary, D., Waters, J., Livesey, N., Froidevaux, L., Lambert, A., Read, W., Filipiak, M. J., and Pumphrey, H. C. (2008). QBO and annual cycle variations in tropical lower stratosphere trace gases from HALOE and Aura MLS observations. *Journal of Geophysical Research: Atmospheres*, 113(D5):n/a–n/a.

Schwartz, M. J., Read, W. G., Santee, M. L., Livesey, N. J., Froidevaux, L., Lambert, A., and Manney, G. L. (2013). Convectively injected water vapor in the North American summer lowermost stratosphere. *Geophysical Research Letters*, 40(10):2316–2321.

Sherwood, S. C., Bony, S., Boucher, O., Bretherton, C., Forster, P. M., Gregory, J. M., and Stevens, B. (2015). Adjustments in the Forcing-Feedback Framework for Understanding Climate Change. *Bulletin of the American Meteorological Society*, 96(2):217–228.

Sherwood, S. C. and Dessler, A. E. (2000). On the control of stratospheric humidity. *Geophysical Research Letters*, 27(16):2513–2516.

Shu, J., Tian, W., Austin, J., Chipperfield, M. P., Xie, F., and Wang, W. (2011). Effects of sea surface temperature and greenhouse gas changes on the transport between the stratosphere and troposphere. *Journal of Geophysical Research*, 116(D2):D02124.

Smalley, K. M., Dessler, A. E., Bekki, S., Deushi, M., Marchand, M., Morgenstern, O., Plummer, D. A., Shibata, K., Yamashita, Y., and Zeng, G. (2017). Contribution of different processes to changes in tropical lower-stratospheric water vapor in chemistryclimate models. *Atmospheric Chemistry and Physics*, 17(13):8031–8044.

Smith, C. J., Kramer, R. J., Myhre, G., Forster, P. M., Soden, B. J., Andrews, T., Boucher, O., Faluvegi, G., Fläschner, D., Hodnebrog, Ø., Kasoar, M., Kharin, V., Kirkevåg, A., Lamarque, J., Mülmenstädt, J., Olivié, D., Richardson, T., Samset, B. H., Shindell, D., Stier, P., Takemura, T., Voulgarakis, A., and WatsonParris, D. (2018). Understanding

Rapid Adjustments to Diverse Forcing Agents. *Geophysical Research Letters*, 45(21).

Smith, J. B., Wilmouth, D. M., Bedka, K. M., Bowman, K. P., Homeyer, C. R., Dykema, J. A., Sargent, M. R., Clapp, C. E., Leroy, S. S., Sayres, D. S., DeanDay, J. M., Paul Bui, T., and Anderson, J. G. (2017). A case study of convectively sourced water vapor observed in the overworld stratosphere over the United States. *Journal of Geophysical Research: Atmospheres*, 122(17):9529–9554.

Solomon, S., Garcia, R. R., Rowland, F. S., and Wuebbles, D. J. (1986). On the depletion of Antarctic ozone. *Nature*, 321(6072):755–758.

Solomon, S., Rosenlof, K. H., Portmann, R. W., Daniel, J. S., Davis, S. M., Sanford, T. J., and Plattner, G.-K. (2010). Contributions of Stratospheric Water Vapor to Decadal Changes in the Rate of Global Warming. *Science*, 327(5970):1219–1223.

Takemura, T., Egashira, M., Matsuzawa, K., Ichijo, H., O'ishi, R., and Abe-Ouchi, A. (2009). A simulation of the global distribution and radiative forcing of soil dust aerosols at the Last Glacial Maximum. *Atmospheric Chemistry and Physics*, 9(9):3061–3073.

Takemura, T., Nozawa, T., Emori, S.and Nakajima, T. Y., and Nakajima, T. (2005). Simulation of climate response to aerosol direct and indirect effects with aerosol transport-radiation model. *Journal of Geophysical Research*, 110(D2):D02202.

Tang, T., Shindell, D., Faluvegi, G., Myhre, G., Olivié, D., Voulgarakis, A., Kasoar, M., Andrews, T., Boucher, O., Forster, P., Hodnebrog, Ø., Iversen, T., Kirkevåg, A., Lamarque, J., Richardson, T., Samset, B., Stjern, C., Takemura, T., and Smith, C. (2019). Comparison of Effective Radiative Forcing Calculations Using Multiple Methods, Drivers, and Models. *Journal of Geophysical Research: Atmospheres*, 124(8):4382–4394.

Tang, T., Shindell, D., Samset, B. H., Boucher, O., Forster, P. M., Hodnebrog, Ø., Myhre, G., Sillmann, J., Voulgarakis, A., Andrews, T., Faluvegi, G., Fläschner, D., Iversen, T., Kasoar, M., Kharin, V., Kirkevåg, A., Lamarque, J.-F., Olivié, D., Richardson, T., Stjern, C. W., and Takemura, T. (2018). Dynamical response of Mediterranean precipitation

to greenhouse gases and aerosols. *Atmospheric Chemistry and Physics*, 18(11):8439–8452.

Thuburn, J. and Craig, G. C. (2002). On the temperature structure of the tropical substratosphere. *Journal of Geophysical Research*, 107(D2):4017.

Ueyama, R., Jensen, E. J., and Pfister, L. (2018). Convective Influence on the Humidity and Clouds in the Tropical Tropopause Layer During Boreal Summer. *Journal of Geophysical Research: Atmospheres*.

Walters, D. N., Williams, K. D., Boutle, I. A., Bushell, A. C., Edwards, J. M., Field, P. R., Lock, A. P., Morcrette, C. J., Stratton, R. A., Wilkinson, J. M., Willett, M. R., Bellouin, N., Bodas-Salcedo, A., Brooks, M. E., Copsey, D., Earnshaw, P. D., Hardiman, S. C., Harris, C. M., Levine, R. C., MacLachlan, C., Manners, J. C., Martin, G. M., Milton, S. F., Palmer, M. D., Roberts, M. J., Rodríguez, J. M., Tennant, W. J., and Vidale, P. L. (2014). The Met Office Unified Model Global Atmosphere 4.0 and JULES Global Land 4.0 configurations. *Geoscientific Model Development*, 7(1):361–386.

Wang, P. K. (2003). Moisture plumes above thunderstorm anvils and their contributions to cross-tropopause transport of water vapor in midlatitudes. *Journal of Geophysical Research*, 108(D6):4194.

Wang, X., Dessler, A. E., Schoeberl, M. R., Yu, W., and Wang, T. (2019). Impact of convectively lofted ice on the seasonal cycle of water vapor in the tropical tropopause layer. *Atmospheric Chemistry and Physics*, 19(23):14621–14636.

Watanabe, M., Suzuki, T., O'ishi, R., Komuro, Y., Watanabe, S., Emori, S., Takemura, T., Chikira, M., Ogura, T., Sekiguchi, M., Takata, K., Yamazaki, D., Yokohata, T., Nozawa, T., Hasumi, H., Tatebe, H., and Kimoto, M. (2010). Improved Climate Simulation by MIROC5: Mean States, Variability, and Climate Sensitivity. *Journal of Climate*, 23(23):6312–6335.

Xia, Y., Huang, Y., Hu, Y., and Yang, J. (2019). Impacts of tropical tropopause warming

on the stratospheric water vapor. *Climate Dynamics*, 53(5-6):3409–3418.

Yang, H., Chen, G., Tang, Q., and Hess, P. (2016). Quantifying isentropic stratosphere-troposphere exchange of ozone. *Journal of Geophysical Research: Atmospheres*, 121(7):3372–3387.

APPENDIX A

Please see a table in the next page that listed values of TOA ERF (Wm^{-2}), ΔTs (K), $\Delta Ts/ERF$ ($K/(Wm^{-2})$), ΔSWV_{slow} (ppmv), $\Delta SWV_{slow}/ERF$ ($ppmv/(Wm^{-2})$), ΔSWV_{fast} (ppmv), and $\Delta SWV_{fast}/ERF$ ($ppmv/(Wm^{-2})$) from all models and perturbations and ensemble average.

These values are shown in figures in the main body of the dissertation and are discussed in the main text. Since in the figures it is hard to tell exact values, we list these numbers here for reference of those figures and texts. Detailed computation methods are described in Chapter 2: Method. Values obtained from each perturbation is listed in separated boxes of tables.

Table A.1: TOA ERF (Wm^{-2}), ΔTs (K), ΔTs/ERF ($K/(Wm^{-2})$), ΔSWV_{slow} (ppmv), ΔSWV_{slow}/ERF ($ppmv/(Wm^{-2})$), ΔSWV_{fast} (ppmv), and ΔSWV_{fast}/ERF ($ppmv/(Wm^{-2})$) from all models and perturbations and ensemble average.

$2xCO_2$	ERF	ΔTs	ΔTs/ERF	ΔSWV_{slow}			ΔSWV_{slow}/ERF			ΔSWV_{fast}			ΔSWV_{fast}/ERF		
				TLS	NH LMS	SH LMS	TLS	NH LMS	SH LMS	TLS	NH LMS	SH LMS	TLS	NH LMS	SH LMS
CAM4	3.57	3.15	0.88	0.81	8.29	4.53	0.23	2.33	1.27	-0.02	1.16	-0.01	-0.01	0.33	-0.00
CAM5	4.00	3.83	0.96	1.17	8.29	4.72	0.29	2.07	1.18	0.07	1.76	0.06	0.02	0.44	0.02
HadGEM3	3.64	8.02	2.20	7.15	33.63	19.87	1.96	9.23	5.45	0.11	0.75	-0.04	0.03	0.20	-0.01
HadGEM2	3.73	4.10	1.10	1.21	8.99	3.02	0.33	2.41	0.81	0.12	0.78	-0.07	0.03	0.21	-0.02
CanESM2	3.57	3.97	1.11	0.94	11.26	4.57	0.26	3.15	1.28	-0.23	0.48	0.13	-0.07	0.13	0.04
IPSL-CM5A	3.36	3.83	1.14	2.05	9.80	5.86	0.61	2.91	1.74	0.28	0.62	0.29	0.08	0.18	0.09
MPI-ESM	4.14	2.20	0.53	1.82	8.49	3.87	0.44	2.05	0.93	0.29	1.03	-0.05	0.07	0.25	-0.01
GISS	3.99	2.12	0.53	0.49	2.29	1.51	0.12	0.57	0.38	-0.09	-0.18	-0.14	-0.02	-0.04	-0.04
MIROC-SPRINTARS	3.62	1.47	0.40	0.30	4.16	2.91	0.08	1.15	0.80	-0.17	0.52	-0.02	-0.05	0.14	-0.01
ensemble average	3.74	3.63	0.98	1.77	10.58	5.65	0.48	2.87	1.54	0.04	0.77	0.02	0.01	0.20	0.01

3xCH4	ERF	ΔTs	ΔTs/ERF	ΔSWV_{slow}			ΔSWV_{slow}/ERF			ΔSWV_{fast}			ΔSWV_{fast}/ERF		
				TLS	NH LMS	SH LMS	TLS	NH LMS	SH LMS	TLS	NH LMS	SH LMS	TLS	NH LMS	SH LMS
CAM4	1.23	1.07	0.87	0.33	2.47	1.55	0.27	2.01	1.25	-0.01	-0.01	0.01	-0.01	-0.01	0.00
CAM5	0.96	0.73	0.76	0.34	1.46	0.83	0.35	1.51	0.87	0.24	0.25	0.40	0.25	0.26	0.42
HadGEM3	1.39	2.37	1.70	1.71	7.98	4.86	1.23	5.72	3.49	0.16	0.35	0.05	0.12	0.25	0.04
HadGEM2	1.25	1.43	1.14	0.37	2.62	0.92	0.29	2.10	0.74	0.17	0.27	0.03	0.13	0.22	0.03
CanESM2	1.36	0.78	0.58	-0.01	1.71	0.57	-0.01	1.26	0.42	0.31	0.83	0.21	0.23	0.61	0.15
IPSL-CM5A	1.63	1.50	0.92	0.38	3.21	1.96	0.24	1.97	1.21	0.09	0.24	0.02	0.06	0.15	0.01
MPI-ESM	0.95	0.58	0.61	0.37	1.80	0.54	0.38	1.90	0.57	0.28	0.51	0.30	0.29	0.54	0.32
GISS	1.34	0.42	0.32	0.11	0.43	0.41	0.08	0.32	0.31	-0.05	-0.26	-0.37	-0.04	-0.19	-0.28
MIROC-SPRINTARS	0.78	0.28	0.35	0.00	0.81	0.55	0.00	1.04	0.70	0.34	0.34	0.32	0.43	0.44	0.41
ensemble average	1.21	1.02	0.81	0.40	2.50	1.36	0.32	1.98	1.06	0.17	0.28	0.11	0.16	0.25	0.12

Table A.1 continued

2%Solar	ERF	ΔTs	ΔTs/ERF	ΔSWV_{slow}			ΔSWV_{slow}/ERF			ΔSWV_{fast}			ΔSWV_{fast}/ERF		
				TLS	NH LMS	SH LMS	TLS	NH LMS	SH LMS	TLS	NH LMS	SH LMS	TLS	NH LMS	SH LMS
CAM4	3.95	2.83	0.72	0.91	7.83	4.92	0.23	1.98	1.24	0.16	1.59	0.20	0.04	0.40	0.05
CAM5	4.32	3.54	0.82	1.20	9.11	5.30	0.28	2.11	1.23	0.19	1.46	0.30	0.04	0.34	0.07
HadGEM3	4.36	9.65	2.21	9.34	46.76	27.55	2.14	10.73	6.32	0.21	0.88	0.08	0.05	0.20	0.02
HadGEM2	4.28	3.11	0.73	1.45	8.64	2.78	0.34	2.02	0.65	0.27	0.89	0.20	0.06	0.21	0.05
CanESM2	4.09	3.02	0.74	1.43	13.34	5.06	0.35	3.26	1.24	0.22	1.11	0.37	0.05	0.27	0.09
IPSL-CM5A	4.11	4.49	1.09	3.33	13.07	7.36	0.81	3.18	1.79	0.23	0.76	0.32	0.06	0.19	0.08
MPI-ESM	4.12	2.81	0.68	1.64	9.17	3.51	0.40	2.23	0.85	0.45	1.43	0.52	0.11	0.35	0.13
GISS	4.48	1.85	0.41	0.52	2.21	1.67	0.12	0.49	0.37	0.09	0.39	0.17	0.02	0.09	0.04
MIROC-SPRINTARS	4.15	1.36	0.33	0.18	4.61	3.64	0.04	1.11	0.88	0.20	0.69	0.21	0.05	0.17	0.05
ensemble average	4.21	3.63	0.86	2.22	12.75	6.87	0.52	3.01	1.62	0.22	1.02	0.27	0.05	0.25	0.06

10xBC	ERF	ΔTs	ΔTs/ERF	ΔSWV_{slow}			ΔSWV_{slow}/ERF			ΔSWV_{fast}			ΔSWV_{fast}/ERF		
				TLS	NH LMS	SH LMS	TLS	NH LMS	SH LMS	TLS	NH LMS	SH LMS	TLS	NH LMS	SH LMS
CAM4	0.77	0.43	0.55	0.06	2.40	0.54	0.08	3.12	0.70	0.63	3.33	0.76	0.82	4.32	0.99
CAM5	0.43	0.38	0.89	-0.10	1.07	0.06	-0.24	2.48	0.15	0.66	2.49	0.55	1.52	5.77	1.28
HadGEM3	0.70	1.19	1.72	1.05	5.86	2.20	1.51	8.44	3.17	0.47	0.80	0.14	0.68	1.15	0.20
HadGEM2	3.17	2.14	0.68	1.62	6.09	1.44	0.51	1.92	0.46	3.27	5.58	0.93	1.03	1.76	0.30
CanESM2	1.55	1.77	1.14	-0.03	6.22	1.72	-0.02	4.01	1.11	1.99	2.56	1.70	1.28	1.65	1.09
IPSL-CM5A	0.81	1.47	1.81	0.38	4.09	1.31	0.47	5.03	1.61	1.28	2.42	0.81	1.57	2.98	1.00
GISS	1.23	0.46	0.37	0.16	1.41	0.30	0.13	1.14	0.24	0.30	0.97	0.42	0.24	0.79	0.34
MIROC-SPRINTARS	0.63	0.13	0.20	-0.06	-0.04	0.37	-0.10	-0.06	0.59	0.28	0.97	0.15	0.44	1.54	0.24
ensemble average	1.16	1.00	0.92	0.38	3.39	0.99	0.29	3.26	1.00	1.11	2.39	0.68	0.95	2.50	0.68

$5xSO_4$	ERF	ΔTs	ΔTs/ERF	ΔSWV_{slow}			ΔSWV_{slow}/ERF			ΔSWV_{fast}			ΔSWV_{fast}/ERF		
				TLS	NH LMS	SH LMS	TLS	NH LMS	SH LMS	TLS	NH LMS	SH LMS	TLS	NH LMS	SH LMS
CAM4	-2.16	-1.49	0.69	-0.37	-3.33	-1.37	0.17	1.54	0.64	-0.01	-1.12	-0.09	0.00	0.52	0.04
CAM5	-2.10	-1.79	0.85	-0.27	-4.25	-2.41	0.13	2.02	1.15	-0.07	-0.06	0.50	0.03	0.03	-0.24
HadGEM3	-8.26	-6.70	0.81	-3.85	-15.69	-11.99	0.47	1.90	1.45	-0.10	-1.03	-0.09	0.01	0.12	0.01
HadGEM2	-3.84	-5.06	1.32	-1.53	-5.69	-1.51	0.40	1.48	0.39	-0.54	-1.00	-0.13	0.14	0.26	0.03
CanESM2	-3.25	-4.45	1.37	-0.51	-8.43	-2.26	0.16	2.60	0.70	-0.01	-0.63	-0.04	0.00	0.19	0.01
IPSL-CM5A	-2.75	-1.99	0.73	-0.78	-6.58	-4.01	0.29	2.40	1.46	0.08	-0.21	0.01	-0.03	0.08	-0.00

Table A.1 continued

$5xSO_4$	ERF	ΔTs	ΔTs/ERF	ΔSWV_{slow}			ΔSWV_{slow}/ERF			ΔSWV_{fast}			ΔSWV_{fast}/ERF		
				TLS	NH LMS	SH LMS	TLS	NH LMS	SH LMS	TLS	NH LMS	SH LMS	TLS	NH LMS	SH LMS
GISS	-2.79	-1.40	0.50	-0.28	-1.58	-0.72	0.10	0.56	0.26	0.02	-0.19	0.00	-0.01	0.07	-0.00
MIROC-SPRINTARS	-2.77	-2.12	0.77	-0.32	-3.85	-1.71	0.11	1.39	0.62	0.01	-0.66	-0.09	-0.00	0.24	0.03
ensemble average	-3.49	-3.13	0.88	-0.99	-6.18	-3.25	0.23	1.74	0.83	-0.08	-0.61	0.01	0.02	0.19	-0.01

10xCFC12	ERF	ΔTs	ΔTs/ERF	ΔSWV_{slow}			ΔSWV_{slow}/ERF			ΔSWV_{fast}			ΔSWV_{fast}/ERF		
				TLS	NH LMS	SH LMS	TLS	NH LMS	SH LMS	TLS	NH LMS	SH LMS	TLS	NH LMS	SH LMS
CAM4	1.54	1.34	0.87	0.43	3.01	1.84	0.28	1.96	1.20	0.21	0.47	0.30	0.13	0.31	0.19
CAM5	1.34	1.00	0.74	0.40	3.76	1.31	0.30	2.81	0.98	0.36	0.80	0.47	0.27	0.60	0.35
HadGEM3	1.51	2.70	1.78	2.17	9.50	5.39	1.43	6.27	3.56	0.37	0.66	0.23	0.24	0.44	0.15
HadGEM2	1.45	1.47	1.01	0.31	2.46	1.18	0.21	1.69	0.81	0.48	0.38	0.27	0.33	0.26	0.18
GISS	1.27	0.44	0.34	0.09	0.52	0.50	0.07	0.41	0.39	0.12	0.22	0.15	0.09	0.17	0.12
MIROC-SPRINTARS	1.20	0.48	0.40	0.07	1.27	0.86	0.06	1.06	0.72	0.32	0.42	0.15	0.27	0.35	0.13
ensemble average	1.39	1.24	0.86	0.58	3.42	1.85	0.39	2.37	1.28	0.31	0.49	0.26	0.22	0.35	0.19

10xCFC11	ERF	ΔTs	ΔTs/ERF	ΔSWV_{slow}			ΔSWV_{slow}/ERF			ΔSWV_{fast}			ΔSWV_{fast}/ERF		
				TLS	NH LMS	SH LMS	TLS	NH LMS	SH LMS	TLS	NH LMS	SH LMS	TLS	NH LMS	SH LMS
HadGEM2	1.20	1.43	1.20	0.69	3.24	0.85	0.58	2.70	0.71	0.37	0.34	0.24	0.31	0.29	0.20
MIROC-SPRINTARS	1.15	0.44	0.38	0.15	1.69	1.12	0.13	1.47	0.98	0.29	0.16	0.38	0.25	0.14	0.33
ensemble average	1.21	0.94	0.79	0.42	2.47	0.99	0.35	2.09	0.84	0.33	0.25	0.31	0.28	0.21	0.26

Table A.1 continued

$3xN_2O$	ERF	ΔTs	ΔTs/ERF	ΔSWV_{slow}			ΔSWV_{slow}/ERF			ΔSWV_{fast}			ΔSWV_{fast}/ERF		
				TLS	NH LMS	SH LMS	TLS	NH LMS	SH LMS	TLS	NH LMS	SH LMS	TLS	NH LMS	SH LMS
CAM4	1.42	1.09	0.77	0.32	2.53	1.65	0.23	1.79	1.17	-0.00	0.17	-0.09	-0.00	0.12	-0.06
HadGEM2	2.19	1.46	0.67	0.73	3.58	1.47	0.33	1.63	0.67	0.43	0.40	0.26	0.20	0.18	0.12
MIROC-SPRINTARS	1.42	0.57	0.40	0.13	1.54	1.55	0.09	1.08	1.09	0.04	-0.00	-0.38	0.03	-0.00	-0.27
ensemble average	1.68	1.04	0.61	0.39	2.55	1.56	0.22	1.50	0.97	0.16	0.19	-0.07	0.08	0.10	-0.07

$5xO_3$	ERF	ΔTs	ΔTs/ERF	ΔSWV_{slow}			ΔSWV_{slow}/ERF			ΔSWV_{fast}			ΔSWV_{fast}/ERF		
				TLS	NH LMS	SH LMS	TLS	NH LMS	SH LMS	TLS	NH LMS	SH LMS	TLS	NH LMS	SH LMS
MIROC-SPRINTARS	3.46	1.22	0.35	0.19	2.73	2.04	0.06	0.79	0.59	0.67	2.16	2.96	0.19	0.62	0.86

10xBCTAU	ERF	ΔTs	ΔTs/ERF	ΔSWV_{slow}			ΔSWV_{slow}/ERF			ΔSWV_{fast}			ΔSWV_{fast}/ERF		
				TLS	NH LMS	SH LMS	TLS	NH LMS	SH LMS	TLS	NH LMS	SH LMS	TLS	NH LMS	SH LMS
CAM4	0.65	0.26	0.41	0.03	0.89	0.39	0.05	1.37	0.60	0.17	1.29	0.25	0.25	1.99	0.39
GISS	1.22	0.41	0.34	0.09	0.79	0.30	0.07	0.65	0.25	0.07	0.26	0.10	0.06	0.21	0.09
ensemble average	0.93	0.34	0.37	0.06	0.84	0.35	0.06	1.01	0.42	0.12	0.78	0.18	0.16	1.10	0.24